Archives of Biochemistry and Biophysics 765 (2025) 110288

Contents lists available at ScienceDirect

Archives of Biochemistry and Biophysics

journal homepage: www.elsevier.com/locate/yabbi

Structural and functional insights into UDP-N-acetylglucosamine-enolpyruvate reductase (MurB) from *Brucella ovis*

Martha Minjárez-Sáenz [a,b], Maribel Rivero [a,b], Víctor Correa-Pérez [a,b], Sergio Boneta [a,b], Paula Suárez [a,b], Víctor Polo [b,c], Sheila J. Sadeghi [d], Inmaculada Yruela [e], Marta Martínez-Júlvez [a,b,**], Milagros Medina [a,b,*]

[a] Departamento de Bioquímica y Biología Molecular y Celular, Facultad de Ciencias, Universidad de Zaragoza, Zaragoza, Spain
[b] Instituto de Biocomputación y Física de Sistemas Complejos (BIFI) Universidad de Zaragoza, GBsC (Unizar) Join Unit to CSIC, Zaragoza, Spain
[c] Departamento de Química Física, Universidad de Zaragoza, Zaragoza, Spain
[d] Department of Life Sciences and Systems Biology, University of Torino, Italy
[e] Estación Experimental de Aula Dei (EEAD), CSIC and GBsC (Unizar) Join Unit to CSIC, Zaragoza, Spain

ARTICLE INFO

Keywords:
MurB
Brucellosis
Antimicrobial target
Peptidoglycan
Crystallography
MD simulation

ABSTRACT

The peptidoglycan biosynthetic pathway involves a series of enzymatic reactions in which UDP-N-acetylglucosamine-enolpyruvate reductase (MurB) plays a crucial role in catalyzing the conversion of UDP-N-acetylglucosamine-enolpyruvate (UNAGEP) to UDP-N-acetylmuramic acid. This reaction relies on NADPH and FAD and, since MurB is not found in eukaryotes, it is an attractive target for the development of antimicrobials. MurB from *Brucella ovis*, the causative agent of brucellosis in sheep, is characterized here. The FAD cofactor in MurB of *B. ovis* is reduced to the hydroquinone state without semiquinone stabilization with an estimated $E_{ox/hq}$ of −260 mV. MurB from *B. ovis* catalyzes the oxidation of NADPH in a slow process that is positively influenced by the presence of the second product, UNAGEP. The crystallographic structure of the $MurB_{ox}$:UNAGEP complex confirms its folding into three domains and the binding of UNAGEP, positioning its enolpyruvyl group for hydride transfer from FAD. MurB shows a complex thermal unfolding pathway that is influenced by UNAGEP and $NADP^+$, confirming its ability to bind both molecules. Molecular dynamics (MD) simulations predict that the nicotinamide of $NADP^+$ is more stable at the active site than the enolpyruvyl of UNAGEP, and suggests that MurB can simultaneously accommodate NADPH and UNAGEP in the substrate channel, increasing overall protein-ligand flexibility. Sequence and evolutionary analyses show that MurB from *B. ovis* conserves all motifs predicted to be involved in catalysis within the Type IIa family.

1. Introduction

The peptidoglycan (PG) biosynthesis pathway involves a sequence of over twenty enzymatic reactions that constitute a crucial process for bacterial cell wall biogenesis, structural integrity, and resilience against fluctuations in osmotic pressure [1–4]. UDP-N-acetylglucosamine-enolpyruvate reductase, known as MurB (EC 1.3.1.98), is a FAD-dependent enzyme involved in the biosynthesis of the N-acetylglucosamine–N-acetylmuramyl pentapeptide, the main building block of the PG polymer [3,5,6]. MurB catalyzes the reduction of UDP-N-acetylglucosamine-enolpyruvate (UNAGEP) to UDP-N-acetyl muramic acid (UNAM), using the reduction equivalents provided by the coenzyme NADPH. UNAGEP, the substrate of MurB, is provided by the previous enzyme in the PG biosynthetic pathway,

Abbreviations: MurB, UDP-N-acetylglucosamine-enolpyruvate reductase; UNAG, UDP-N-acetylglucosamine; PEP, phosphoenolpyruvate; UNAGEP, UDP-N-acetylglucosamine-enolpyruvate; UNAM, UDP-N-acetylmuramic acid; PG, peptidoglycan; (PDDA) polymer, poly (diallyldimethylammonium chloride); HT, hydride transfer; DTT, DL-dithiothreitol; SEC, size exclusion chromatography; CN-PAGE, Native Polyacrylamide Gel Electrophoresis; (PDA) detector, photodiode array; MD, Molecular Dynamics; MSA, multiple sequence alignment; PDA, photodiode array.

* Corresponding author. Departamento de Bioquímica y Biología Molecular y Celular, Facultad de Ciencias, Universidad de Zaragoza, Zaragoza, Spain.
** Corresponding author. Departamento de Bioquímica y Biología Molecular y Celular, Facultad de Ciencias, Universidad de Zaragoza, Zaragoza, Spain.
E-mail addresses: mmartine@unizar.es (M. Martínez-Júlvez), mmedina@unizar.es (M. Medina).

https://doi.org/10.1016/j.abb.2025.110288
Received 6 October 2024; Received in revised form 27 December 2024; Accepted 3 January 2025
Available online 4 January 2025

UDP-N-acetylglucosamine enolpyruvyl transferase (MurA), that adds the enolpyruvyl moiety from phosphoenolpyruvate (PEP) to UDP-N-acetylglucosamine (UNAG). The MurB catalyzed reaction has been particularly studied in *Escherichia coli*, *Staphylococcus aureus* and *Streptococcus pneumoniae*, being reported to occur through a ping-pong bi-bi mechanism (Fig. 1A) [5,7–14]. In the MurB flavin reductive half-reaction, its FAD cofactor is reduced to the hydroquinone state ($FADH^-$) by hydride transfer (HT) from NADPH. Upon $NADP^+$ release, UNAGEP binds to reduced MurB, and subsequently during the flavin oxidative half-reaction reduction of the vinyl enol ether of UNAGEP produces UNAM. In this reaction, HT from the MurB $FADH^-$ cofactor to the C3 atom of the UNAGEP enolpyruvyl moiety generates a carbanionic intermediate that is then protonated at C2 by a solvent proton [5,8,9]. Due to its essential housekeeping role and the absence of homologues in eukaryotes, bacterial MurB enzymes were proposed as targets for the discovery of antimicrobials [6,15–21]. However, MurB enzymes from nearly all pathogenic bacteria remain widely unexplored and their functional features have not been reported [22]. In addition, there is currently no antimicrobial use for any bacterial MurB as target, despite a few potential inhibitors have been reported [23].

MurB enzymes classify into two major types (**Table SP1**) [24]. The Type I is characterized by a Tyr-loop and a prominent feature that folds into a βαββ architecture in domain III, whereas Type II specifically lacks the aforementioned features. Examples of Type I are MurBs from *E. coli, Mycobacterium tuberculosis* and *Pseudomonas aeruginosa* [25–27]. Type II MurBs are further subdivided into subclasses "IIa" and "IIb", according to the nature of the catalytic residue acting as a proton donor to the carbanion intermediate, which are Ser and Cys, respectively [24]. MurBs of Type IIa are structurally exemplified by those from *S. aureus* [28], *Listeria monocytogenes* [29] or *Bacillus licheniformis* [30], whereas MurB from *Thermus caldophilus* is of Type IIb [31]. MurB is highly conserved within α-proteobacteria [12], and is one of the 42 flavoenzymes belonging to the core proteome in *Brucella* [32].

This work focuses on MurB from *Brucella ovis*. This is a Gram-negative, non-zoonotic pathogenic bacterium with a major economic impact in countries and regions with sheep (*Ovis aries*) breeding

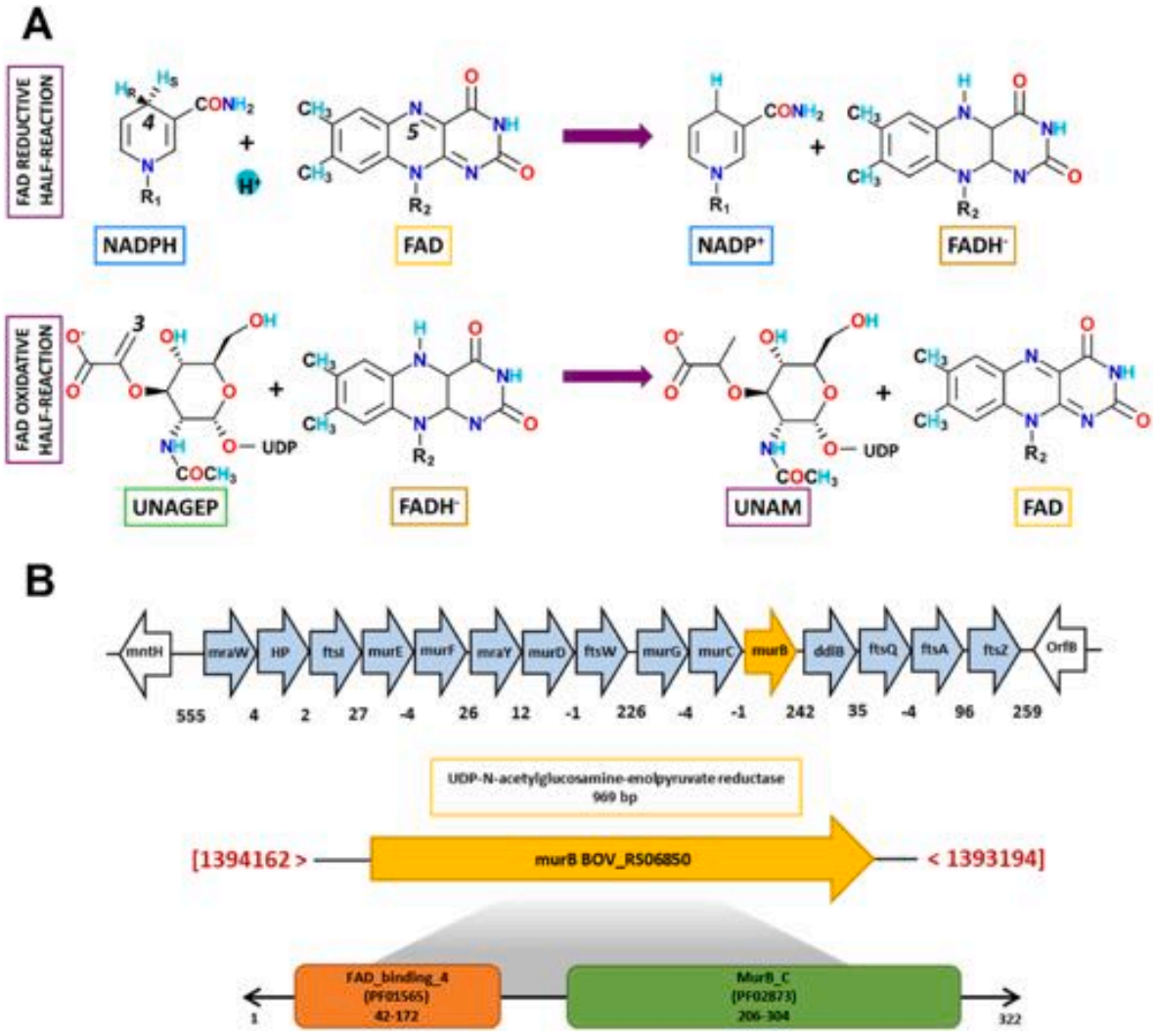

Fig. 1. - Catalytic mechanism in MurB enzymes and *murB* genomic context in *Brucella ovis*. Proposed catalytic mechanism in MurB enzymes. In the flavin reductive half-reaction (top) the MurB FAD cofactor is reduced to $FADH^-$ upon HT from NADPH, whereas in the flavin oxidative half-reaction (bottom) HT from $FADH^-$ to the UNAGEP enolpyruvyl group reduces it to a lactoyl and converts UNAGEP to UNAM. **(B)** Scheme of the *dcw* operon involved in PG biosynthesis where *murB* gene is located in *B. ovis* (top). Genes are shown in light blue with the exception of *murB* that is in yellow, arrowheads indicate the direction of transcription and numbers below genes the intergenic distance (negative numbers indicate overlapping genes). Underneath, the location of *murB* within the genome (NC_009505.1: 1393M–13984 M), accounting for 969 bp (bottom) Two boxes depict the Pfam domains formed by the 322 amino acids present in the final product, the MurB enzyme; the FAD_binding_4 (PF01565, commonly found in enzymes that use FAD, including many oxygen-dependent oxidoreductases), illustrated in orange, and the MurB_C (PF02873, unique to MurB enzymes) in green. (For interpretation of the references to color in this figure legend, the reader is referred to the Web version of this article.)

activities, causing placentitis in sheep and genital lesions in rams, which affect fertility and semen quality [33]. In *B. ovis*, the *murB* gene (NCBI ID 45124764, BOV_RS06850) is part of the division and cell wall (*dcw*) cluster, which contains other genes encoding enzymes involved in PG biosynthesis [32,34] (Fig. 1B). Here, MurB from *B. ovis* has been heterologously produced, and its *in vitro* stability, redox functionality and structural features evaluated. This study provides the first insights into the molecular characterization of the mechanism of action of MurB from *B. ovis*, including the allocation of substrates in its active site, paving the way for future mechanistic studies and further exploration of its potential as a drug target. In addition, it classifies *B. ovis* MurB as Type IIa, and evaluates it within the context of the MurB family in different organisms.

2. Materials and methods

2.1. Cloning, overexpression and purification of MurB from B. ovis

Two constructs for the *B. ovis* ATCC 25840 BOV_RS06850 (*murB*) gene, encoding for the MurB protein (ABQ61769.1), were cloned into the NcoI/BamHI sites of the pET-28a(+) plasmid by GenScript. One of them encoded for the protein residues (hereafter MurB), while the other contained an additional 70 bp extension at the 5′-end encoding a His_6-tag, the PreScission protease cleavage site, and a NdeI restriction site (hereafter His_6MurB). Both pET28a-MurB constructs were used to transform *E. coli* BL21(DE3) competent cells by heat shock at 42 °C. Clones of transformed *E. coli* were selected on LB/agar plates with 30 μg/mL kanamycin and then grown in LB media. Cultures were incubated at 37 °C until $O.D._{600nm}$ reached 0.5. Overexpression was induced by adding 1 mM of isopropyl β-D-1-thiogalactopyranoside, and cultures were further incubated at 30 °C for 5 h. Cells were harvested by centrifugation at 3,500 g for 10 min at 4 °C, washed with 0.15 M NaCl, and stored at −20 °C. For purification of His_6MurB, cells were thawed and resuspended in 75 ml (2 mL/gr cell pellet) cell lysis buffer (50 mM Bis-Tris Propane, pH 7.6, 250 mM KCl, 1 mM DL-dithiothreitol (DTT) and 10 mM imidazole) with ½ tablet of cOmplete™ (Roche). Cells were then disrupted by sonication at 4 °C (10 cycles of 30 s) in a DRH UP200 DR sonicator (Hielscher). Cell debris was removed by centrifugation at 44,800 g for 1 h at 4 °C. To purify His_6MurB, the supernatant was filtered and loaded onto a 5 mL His-Trap™ HP column (Cytiva) equilibrated with cell lysis buffer and connected to the ÄKTA™ system (Cytiva). Unbound proteins were washed with 3 column volumes of the same buffer and then His_6MurB was eluted with a 10–500 mM imidazole gradient in 50 mM Bis-Tris Propane, pH 8.0, 100 mM KCl, 1 mM DTT. Aliquots containing His_6MurB (checked by 12 % SDS/PAGE) were pooled and dialyzed overnight against 50 mM Bis-Tris Propane, pH 8.0, 100 mM KCl, 1 mM DTT. The His_6MurB solution was concentrated using 10 kDa Merck Amicon ultrafiltration devices (Millipore) and further purified by size exclusion chromatography (SEC) using a Superdex 200 10/300 GL column (Cytiva) pre-equilibrated with 50 mM Bis-Tris Propane, pH 8.0, 100 mM KCl, 1 mM DTT buffer. To purify MurB, after sonication and centrifugation, the supernatant was adjusted to 30 % of ammonium sulfate ($(NH_4)_2SO_4$), stirred on ice for 1 h, and centrifuged at 44,800 g for 10 min at 4 °C. The supernatant was then collected, and the procedure was repeated with 60 % and 80 % of ammonium sulfate. In the last step, the appearing yellow precipitate was collected and dissolved in 50 mM Tris/HCl pH 8.0, 0.5 mM DTT and 30 % ammonium sulfate, applied to a DEAE-Sepharose column pre-equilibrated with the same buffer, and eluted with a reverse gradient from 30 % to 0 % of ammonium sulfate in 50 mM Tris/HCl, pH 8.0 and 0.5 mM DTT. The yellow fractions were pooled and dialyzed in 50 mM Tris/HCl, pH 8.0, 0.5 mM DTT. The protein was then applied to a DEAE-Sepharose column, pre-equilibrated with 50 mM Tris/HCl, pH 8.0, 0.5 mM DTT, and eluted with a linear gradient from 0 to 500 mM KCl in the same buffer. The yellow fractions were pooled and dialyzed in 50 mM Tris/HCl, pH 8.0 and 0.5 mM DTT, loaded onto a 5 mL HiTrap™ Q FF column (Cytiva), and eluted with a linear gradient of 0–500 mM KCl. The fractions were pooled and concentrated, and a final SEC purification step was performed as described above for His_6MurB by using 50 mM Tris/HCl pH 8.0, 100 mM KCl and 0.5 mM DTT. SEC,12 % SDS-PAGE and 15 % CN-PAGE were used to assess both protein purity and molecular weight (Mw). Typical yields after purification were ~4.5 mg of MurB per liter of *E. coli* culture. Pure protein fractions were pooled, concentrated, and stored at −80 °C in 50 mM Bis-Tris Propane, 100 mM KCl, pH 8.0, 1 mM DTT until used.

2.2. Production of the UNAGEP substrate of MurB

UNAGEP is not commercially available, so its preparation was carried out in 1 mL solutions containing 200 μM UNAG (Sigma-Aldrich), 660 μM PEP (Roche) and 50 nM MurA from *B. ovis* in 50 mM Bis-Tris Propane, pH 7.5 (this buffer is a requirement for MurA to exhibit activity, unpublished results). The reaction was incubated at 37 °C for 4 h, followed by the addition of 50 nM MurA and further incubation at 37 °C overnight. MurA was then separated using a 10 kDa Merck Amicon ultrafiltration device (Millipore), and the eluate containing the reaction products was concentrated using a Savant SpeedVac (Thermo Scientific). The amounts of UNAG/UNAGEP in these solutions was quantified for UDP by measuring its absorbance at 262 nm (ε_{262nm} = 9.8 $mM^{-1}cm^{-1}$). The formation of UNAGEP was confirmed by NMR. ^{1}H and ^{13}C NMR spectra were recorded at the NMR Research Support Service of the Instituto de Síntesis Química y Catálisis Homogénea (iSQCH, University of Zaragoza).

2.3. Spectroscopic characterization

UV–Vis spectra were routinely recorded in 50 mM Bis-Tris Propane, 100 mM KCl pH 8.0, 1 mM DTT at 25 °C, using either a Specord 200 Plus (Analytik Jena) or a CARY 3500 (Agilent Technologies) spectrophotometer. The molar extinction coefficient for MurB in the flavin band-I (ε_{463nm}) was determined spectrophotometrically by thermal denaturation of the protein for 10 min at 90 °C, followed by centrifugation to separate the precipitated apo-protein, and spectroscopic quantification of the FAD released to the supernatant as previously described [35]. The ability of MurB to be photoreduced by photoirradiation in protonated buffers was evaluated in samples containing 20 μM of the protein in 50 mM Bis-Tris Propane, 100 mM KCl, pH 8.0, 1 mM DTT, 20 % glycerol and 50 mM EDTA in a closed anaerobic cuvette. Anaerobic conditions were achieved by several cycles of evacuation and bubbling with O_2-free argon in a Schlenk line system [36]. Each sample was then stepwise photoirradiated for 5 s periods with a blue LED strip tube that provides an intensity of 900 μmol photons/(m^2.s) around the cuvette. Photoreduction was followed by recording Vis spectra after each irradiation by using a CARY 3500 spectrophotometer (Agilent Technologies). Potential changes in the FAD cofactor environment upon $NADP^+$ binding to MurB samples were investigated by difference spectroscopy, titrating the protein with increasing concentrations of $NADP^+$ as previously described [37]. Fluorescence spectra were monitored using a Cary Eclipse fluorimeter (Agilent Technologies) with 10–20 μM of protein and a scan speed of 5 nm/s, using quartz cells of 1 cm of optical path length. Circular dichroism (CD) spectra were recorded on a Chirascan spectropolarimeter (Applied Photophysics Ltd.) with 0.5 nm/s steps and 8 s of measurement time per point. Far-UV (200–260 nm) and near-UV/Vis (260–700 nm) CD spectra were registered in 0.1 and 1 cm path length cuvettes, respectively, with MurB at ~5 μM for far-UV and 20 μM for near-UV. Fluorescence and CD measurements were performed in 10 mM potassium phosphate (KPi), pH 8.0, at 10 °C.

2.4. Determination of the midpoint reduction potential for the FAD cofactor of MurB and of the MurB ability to conduct current to UNAGEP

The reduction of MurB by the xanthine/xanthine oxidase (XO)

method [38,39] was carried out in a closed anaerobic cuvette with a final concentration of ~10 μM of His_6MurB, 2 μM benzyl viologen, 500 μM xanthine, 5 μM of the phenosafranine dye (E_m = -252 mV), 10 mM glucose and 10 U/mL glucose oxidase, in 50 mM Bis-Tris Propane pH 8.0, 100 mM KCl, 1 mM DTT. After achieving anaerobic conditions, as indicated above using an anaerobic cuvette and a Schlenk line, 7.8 μg/mL of bovine milk XO (Sigma-Aldrich) were added from the side arm to the mixture in the cuvette, and spectra were recorded every 5 min scanning from 350 to 700 nm at 25 °C, in a CARY 3500 spectrophotometer (Agilent Technologies). To ensure thorough equilibration of the components during the experiment, the concentration of XO was set at 30 nM (within the recommended range of 1–100 nM) allowing the reductive process to proceed over a period of 2–3 h. The absorbance changes accompanying reduction of the indicator dye at 525 nm and of the flavoprotein at 412 nm at each time point during the xanthine/XO reduction were used to determine the MurB $E_{ox/hq}$ value using the Nernst equation as previously reported [38,39]. Cyclic voltammetry (CV) measurements were performed using an Autolab PGSTAT12 potentiostat controlled by the GPES3 software (Ecochemie, The Netherlands). The 1 mL glass electrochemical cell was equipped with a platinum wire counter electrode, an Ag/AgCl (3 M NaCl, E_m = +220 mV) reference electrode and a 3 mm diameter glassy carbon working electrode (BASi, USA). The glassy carbon electrode was modified with a mixture of the protein and poly (diallyldimethylammonium chloride) (PDDA) polymer as follows: 5 μL of PDDA was mixed with 5 μL of His_6MurB (147 μM) and drop coated onto the electrode [40]. The modified bioelectrode was stored at 4 °C overnight. The CV measurements were carried out at 25 °C under anaerobic conditions obtained by flushing the samples under a nitrogen saturated atmosphere. The potential was scanned between 0 and -700 mV at a scan rate of 120 mV/s. Control experiments were carried out in the absence of the protein with buffer. Additionally, FAD was immobilized onto the electrode and subjected to scanning in the same manner as the protein solution. The supporting electrolyte was 50 mM KPi buffer, 100 mM KCl, pH 7.4. CV was also used to evaluate the ability of the electrochemically reduced MurB to transfer electrons to UNAGEP. For these measurements, His_6MurB (73.5 μM) was incubated with UNAGEP (~1 mM) for 3 h, at 4 °C. 10 μL of this mixture was drop coated on the glassy carbon electrode and covered with 5 μL of PDDA. The modified electrode was stored at 4 °C overnight. In this case, CV measurements were carried out by applying a potential between −150 and −650 mV at a lower scan rate of 5 mV/s. Chronoamperometry was also used to measure changes in the current over time upon titrating His_6MurB with UNAGEP. For these experiments, the glassy carbon electrode was modified using a mixture of the His_6MurB (147 μM) and PDDA as described above. Measurements were carried out under nitrogen atmosphere by applying a potential bias of −700 mV for 20 min at 25 °C. At two different time points during the chronoamperometry (3 and 8 min) 25 μL of UNAGEP (~3 mM) were titrated into the electrochemical glass cell and the increase in the current recorded. HPLC was used to confirm transformation of UNAGEP into UNAM in reaction mixtures containing MurB and UNAGEP and resulting from the CV and chronoamperometry experiments. HPLC was performed at 25 °C using an Alliance Waters 2707 autosampler, with a Waters 2996 photodiode array (PDA) detector and a Waters HSST3 C18 column (4.6 × 50 mm, 3.5 mm), preceded by a precolumn (4.6 × 20 mm, 3.5 mm) of the same material, using as mobile phase 5 % methanol (vol/vol) in 5 mM ammonium acetate, pH 4.0.

2.5. Kinetic methods to evaluate the MurB redox functionality

The ability of MurB and His_6MurB to oxidize NADPH was analyzed by monitoring changes in absorbance in the 300–600 nm range in a CARY 3500 spectrophotometer (Agilent Technologies) to evaluate for both coenzyme oxidation and FAD spectroscopic properties during turnover. A screening of different experimental conditions was conducted in order to detect activity: including enzyme, NADPH and UNAGEP concentrations, working buffers, pH values, presence of univalent and divalent cations, NADH instead of NADPH, temperatures, glycerol presence, reaction times, and aerobic/anaerobic conditions. In summary, all conditions previously reported in the literature for assessing MurB activity in other species were tested [5,8,9,11,12,41].

Reduction of the FAD cofactor of MurB was also evaluated by fast kinetic stopped-flow by using a SX.18 MV spectrophotometer (Applied Photophysics Ltd.) interfaced with a PDA detector according to established protocols [36]. To follow the reduction kinetics, anaerobic solutions containing MurB (10–16 μM) in the absence or presence of UNAGEP (200 μM), NADPH (200 μM) and sodium dithionite ($Na_2S_2O_4$, 300 μM) were produced. These samples were loaded into separate stopped-flow syringes and then mixed as indicated in the results section in a 1:1 ratio in 50 mM Bis-Tris Propane pH 8.0, 100 mM KCl, 1 mM DTT at 25 °C, all under anaerobic conditions. To follow the kinetics of photoreduction of MurB within the stopped-flow chamber, an anaerobic protein solution (10 μM) was prepared in 50 mM Bis-Tris Propane pH 8.0, 100 mM KCl, 1 mM DTT, 20 % glycerol and 50 mM EDTA and then mixed 1:1 with the same anaerobic buffer. The mixture was then exposed to photoirradiation from the instrument source lamp (150 W/CR OFR Xenon Short Arc Lamp, OSRAM) in the reaction chamber for long periods of time (up to 8000 s). In all cases, multiple wavelength absorption data (400–700 nm) were collected. Observed rate constants (k_{obs}), as well as potentially interesting spectroscopic properties of intermediate species, were determined by fitting absorption decays at 462 nm, as a combination of exponential or linear processes, as well as by deconvolution of time spectral evolutions by global analysis and numerical integration methods using Pro-Kineticist (Applied Photophysics Ltd.) [36]. The estimated error of the determined rate constant values was ±15 %.

2.6. Thermal denaturation assays for MurB stability study

The thermal stability of MurB samples, both in the absence and presence of ligands, was evaluated by following changes in the far-UV CD (at 222 nm) as well as in the tryptophan and FAD fluorescence emission bands upon increasing temperature. Denaturation curves were recorded from 10 to 90 °C (283.15–363.15 K) in 10 mM KP_i pH 8.0, with scan rates of 1 and 1.5 °C/min for CD and fluorescence assays, respectively. The MurB concentration was 5 μM for far-UV CD assays (signals recorded at 222 nm in a 0.1 cm path length cuvette), while samples containing 10 μM of MurB were used when following tryptophan (λ_{ex} = 280 nm and λ_{em} = 330 nm) and FAD (λ_{ex} = 460 nm and λ_{em} = 527 nm) fluorescence. When present, UNAG and UNAGEP were in a 10-fold excess, while $NADP^+$/H was in 20-fold excess.

Individual experimental data sets were globally analyzed as one-transition (native↔unfolded, N↔U), two-transition (native-↔intermediate↔unfolded, N↔I↔U) or three-transition processes (native↔intermediate1↔intermediate2↔unfolded, N↔I_1↔I_2↔U) by applying the following equations [42]:

$$S_{obs} = \frac{S_N + m_N T + (S_U + m_U T) e^{-\left(\frac{\Delta G}{RT}\right)}}{1 + e^{-\left(\frac{\Delta G}{RT}\right)}} \quad \text{Eq. 1}$$

$$S_{obs} = \frac{S_N + m_N T + (S_I + m_I T)\, e^{-\left(\frac{\Delta G_1}{RT}\right)} + (S_U + m_U T) e^{-\left(\frac{(\Delta G_1 + \Delta G_2)}{RT}\right)}}{1 + e^{-\left(\frac{\Delta G_1}{RT}\right)} + e^{-\left(\frac{(\Delta G_1 + \Delta G_2)}{RT}\right)}} \quad \text{Eq. 2}$$

$$S_{obs} = \frac{S_N + m_N T + (S_{I1} + m_{I1} T)\, e^{-\left(\frac{\Delta G_1}{RT}\right)} + (S_{I2} + m_{I2} T)\, e^{-\left(\frac{(\Delta G_1 + \Delta G_2)}{RT}\right)} + (S_U + m_U T) e^{-\left(\frac{(\Delta G_1 + \Delta G_2 + \Delta G_3)}{RT}\right)}}{1 + e^{-\left(\frac{\Delta G_1}{RT}\right)} + e^{-\left(\frac{(\Delta G_1 + \Delta G_2)}{RT}\right)} + e^{-\left(\frac{(\Delta G_1 + \Delta G_2 + \Delta G_3)}{RT}\right)}} \quad \text{Eq. 3}$$

where S_{obs} is the measured protein signal at a given temperature (T), S_N, S_{I1}, S_{I2}, and S_U are the signals (origin intercept) of native, intermediate and unfolded protein conformations at 0 K, respectively, and m_N, m_{I1}, m_{I2}, and m_U are the slopes of the linear temperature dependence of those signals. The free energy difference in Eq. (1) or Eq. (2) follows, $\Delta G_i = \Delta H_i\left(1 - \frac{1}{T_{mi}}\right) + \Delta C_{Pi}\left(T - T_{mi} - T\ln\frac{T}{T_{mi}}\right)$, where ΔH_i, T_{mi} and ΔC_{Pi} are the van't Hoff enthalpy, the mid-transition temperature and the heat capacity change for each unfolding transition, and R is the ideal gas constant.

2.7. Crystallization and structure resolution of MurB

Initial crystallization trials of MurB samples were performed using commercial screens as JBScreen Classic, JBScreen Basic, JBScreen PEG/Salt and JBScreen JCSG ++ (Jena Bioscience), as well as Morpheus and MIDAS (Molecular Dimensions). Typically, 0.5 μL of 10 mg/mL of MurB in 50 mM Tris/HCl pH 8.0, 100 mM KCl, 1 mM DTT were mixed with 0.5 μL of each condition, and equilibrated against 60 μL of the precipitating solution. Crystals of the complex were obtained in a solution of MurB (25 mg/mL) with UNAGEP (1 mM, produced as above indicated) in the C1 condition of the JBScreen Classic HTS (16 % PEG 4000, 200 mM lithium sulfate, 100 mM Tris/HCl, pH 8.5). Crystals grew in 4 days and were cryoprotected with 20 % ethylene glycol and cooled to 100 K with liquid nitrogen. Diffraction data from a single crystal of the $MurB_{ox}$:UNAGEP complex were collected using a Dectris Pilatus 6 M detector at the BL13-XALOC beamline of ALBA, Barcelona (Spain), to a maximum resolution of 2.10 Å. The best data set was processed, scaled and reduced with XDS [43] and SCALA [44] from the CCP4 package [45,46]. The structure was solved by molecular replacement using the MOLREP program [47] from CCP4 and the AlphaFold [48] model for MurB from *B. ovis* (code A5VRH5) as a search template. Automatic refinement was performed by REFMAC5 [49] from CCP4 and alternating manual model building by COOT [50]. Final refinement steps were performed using refine from PHENIX [51]. The final model included residues 1–322, one FAD, one UNAGEP (identified as EPU), and 120 water molecules. Molprobity [52] was used to assess the final structure quality. Relevant data collection statistics and refinement parameters are presented in **Table SP2**. The coordinates and structure factors for the $MurB_{ox}$:UNAGEP complex are deposited in the Protein Data Bank under the accession code 9DTK.

2.8. Molecular dynamics (MD) simulations

To evaluate the potential dynamics of the interaction of MurB from *B. ovis* with its substrates four structural models were produced (**Figure SP1**): (i) free MurB with oxidized FAD cofactor (hereafter FAD) ($MurB_{ox}$), (ii) MurB with FAD in the anionic hydroquinone state (hereafter $FADH^-$) and in complex with UNAGEP ($MurB_{hq}$:UNAGEP), (iii) MurB with FAD and in complex with NADPH ($MurB_{ox}$:NADPH), and (iv) MurB with FAD and in complex with both UNAGEP and NADPH ($MurB_{ox}$:NADPH:UNAGEP). Structural models were derived from former crystallographic and AlphaFold data. The NADPH position was adjusted considering the $MurB_{ox}$:$NADP^+$ complex from *P. aeruginosa* (PDB ID 4JAY and 4JB1), while for UNAGEP the structure here presented (PDB ID 9DTK) as well as that MurB from *T. caldophilus* (PDB ID 2GQU) were considered. Before initiating any MD simulation, the structural models were meticulously prepared. This involved the removal of all crystallographic water molecules and the fine-tuning of the protonation of residues at pH 7.0 utilizing the PROPKA software [53]. MD simulations were carried out using GROMACS 2018.4 software [54], and the protein parameters were defined with the AMBER ff03 force field [55]. Standard residue topologies were assigned using the GROMACS pdb2gmx tool, while FAD, $FADH^-$, UNAGEP and NADPH molecules were parameterized using *ab initio* methods. Charges for each atom were determined through the restrained electrostatic potential (RESP) technique using Multiwfn [56], following structure optimization at the HF/6-31G(d,p) level in Gaussian 09 [57]. These charges served as the initial parameters for the subsequent parameterization using the GAFF force field [58] via ACPYPE [59]. To set periodic boundary conditions, the system was enclosed within a rhombic dodecahedron box. Explicit water molecules were modeled using the TIP3P model. The system was neutralized by replacing random solute molecules with sodium ions. Prior to running production simulations, the studied systems underwent steepest descent minimization to alleviate close contacts or clashes. Equilibration was achieved through short 100 ps simulations under the NVT ensemble, with initial velocities generated according to a Boltzmann distribution at 310 K. Subsequently, a 100 ps simulation under the NPT ensemble at 1 atm was conducted. During both equilibration stages, harmonic potentials with a force constant of 1000 kJ/(mol·nm) were applied to restrict the movement of the heavy atoms in the protein and ligand. Once the desired equilibrated conditions were met, the productive MD phase began with unrestrained positions for all atoms except hydrogen atoms, which were constrained using the LINCS algorithm [60]. Simulations were performed under an NPT ensemble at 310 K with a leap-frog integrator using 2 fs time steps, and data were collected every 10 ps. Long-range electrostatic interactions were computed using the Particle Mesh Ewald method, pressure was controlled via the Parrinello-Rahman method, and temperature equilibration was maintained through a modified Berendsen scheme. The simulations extended up to 100 ns, and each trajectory was replicated twice. All MD simulations were executed on the CESAR supercomputer at BIFI. Analysis of the simulations was performed using custom scripts that use GROMACS tools, the MDTraj library [61] and PyMOL [62].

2.9. Sequence and structural analysis

The NCBI database [63] was used to analyze the genetic context of BOV_RS06850 (*murB* gene). MurB-related amino acid sequences in the α-proteobacteria family and in other phyla were found, using the server PSI-Blast, and PDB (https://www.rcsb.org/) and NCBI (https://www.ncbi.nlm.nih.gov/) as search databases. All this information was supplemented and supported by UniProt (https://www.uniprot.org/). The protein domains were identified using InterPro server [64]. The Logo sequence was generated with WebLogo (https://weblogo.berkeley.edu/) [65]. Multiple sequence alignments (MSAs) were produced using ClustalW within MEGA11 software [66] and Clustal Omega (https://www.ebi.ac.uk/jdispatcher/msa/clustalo). Phylogenetic trees were constructed using the Maximum Likelihood (ML) method and the JTT matrix-based model [67] within MEGA11 and NGPhylogeny [68–70]. 500 or 1000 bootstrap replicates were conducted during the construction of each phylogenetic tree to test the confidence or reliability of the

branches. Initial tree(s) for the heuristic search were obtained automatically by applying Neighbor-Join and BioNJ algorithms to a matrix of pairwise distances estimated using the JTT model, and then selecting the topology with superior log likelihood value. The trees and cladograms were midpoint-rooted and plotted with FigTree (http://tree.bio.ed.ac.uk/software/figtree/). The algorithm TM-align [71] was used for protein structure comparisons. PyMol software was used to visualize and generate structural figures [62].

3. Results

3.1. Spectroscopic and redox properties of recombinant MurB from B. ovis

The absorption spectra of the purified MurB and His_6MurB forms exhibited maxima at 270, 380 and 463 nm (last two characteristic bands II and I of the flavin cofactor, respectively), and a shoulder at 489 nm (Fig. 2A). Extinction coefficients of MurB and His_6MurB were respectively determined as $\varepsilon_{463nm} = 11.6 \pm 0.4$ $mM^{-1}cm^{-1}$ and $\varepsilon_{463nm} = 12.1 \pm 0.3$ $mM^{-1}cm^{-1}$ in 50 mM Bis-Tris Propane pH 8.0, 100 mM KCl, 1 mM DTT. Protein denaturation identified FAD in the supernatant as the sole non-covalent compound that binds to MurB and absorbs in the UV–Vis region (Fig. 2A). When purified to homogeneity, MurB shows an Abs_{270nm}/Abs_{463nm} value around 5.5, in agreement with the low tryptophan content of the protein (W34, W242 and W300 residues). The determined theoretical Abs_{280nm} (considering a theoretical extinction coefficient contributed by the unfolded protein plus that of FAD and the protein concentration as evaluated from Abs_{463nm}) differed less than 10 % from the experimental value. Given that extinction coefficients for protein and flavin at 280 nm may change upon holoprotein formation, the FAD:protein ratio can be assumed to be close to 1:1. Both MurB forms accepted electrons through photoirradiation by undergoing FAD photoreduction (Fig. 2B), recovering the original oxidized spectrum upon exposure to molecular oxygen. No evidence of FAD semiquinone stabilization was observed during flavin reductive and oxidative processes, and an isosbestic point at 341 nm was observed during the reductive process. MurB and His_6MurB also exhibited similar fluorescence emission spectra, with maxima at 331 and 528 nm upon excitation in the tryptophan (280 nm) and flavin band I (460 nm) regions, respectively (Fig. 2C–D). Fluorescence quantum yields of MurB in both spectroscopic regions were slightly higher than those of His_6MurB, suggesting that the His-tail somehow quenches the tryptophan and FAD

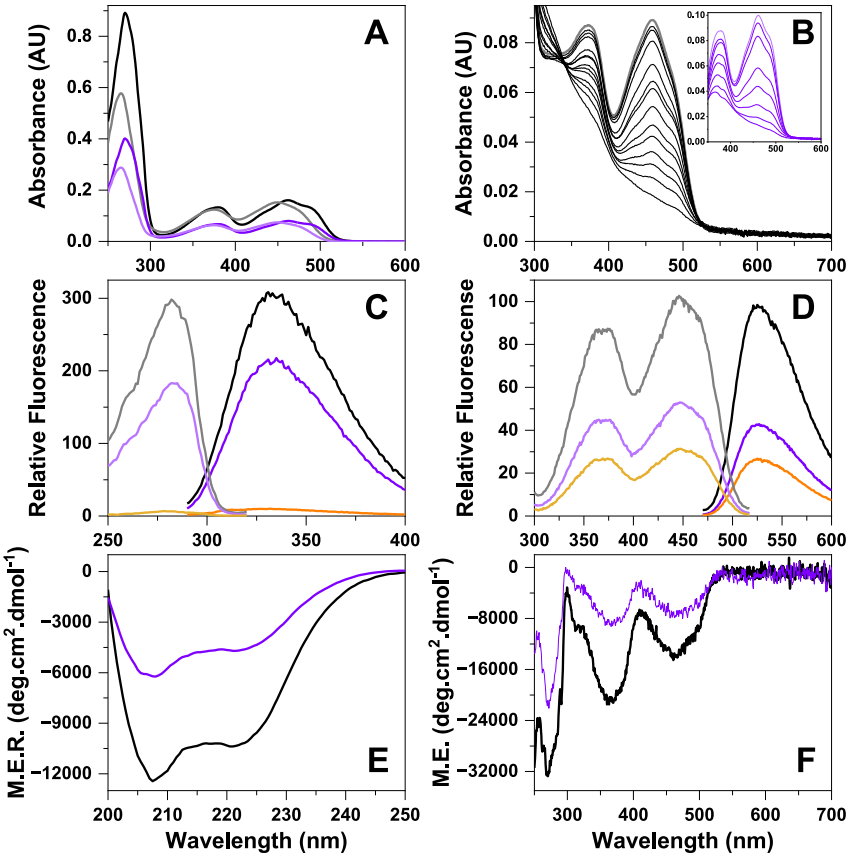

Fig. 2. - Spectral properties of MurB from *B. ovis*. **(A)** UV–Vis absorption spectrum of MurB (14 μM) (black line) and His_6MurB (6.5 μM, violet line) in 50 mM Bis-Tris Propane pH 8.0, 100 mM KCl, 1 mM DTT at 25 °C, and of their released FAD cofactors (respectively grey and light violet lines) upon incubation for 5 min at 90 °C. **(B)** Spectral evolution for the photoreduction of MurB (8 μM) and His_6MurB (8.5 μM, inset) in the visible region. Spectra recorded in 50 mM Bis-Tris Propane pH 8.0, 100 mM KCl, 1 mM DTT, 20 % glycerol, 50 mM EDTA at 25 °C. Emission fluorescence spectra of MurB (7.8 μM, black line), His_6MurB (7.9 μM, violet line) and free FAD (7.9 μM, orange line) in the **(C)** tryptophan region, $\lambda_{ex} = 280$ nm and in the **(D)** flavin region, $\lambda_{ex} = 460$ nm. The excitation spectra (respectively grey, light violet, and light orange lines) are shown when collecting emission at 330 and 528 nm, for panel C and D, respectively. In all cases, fluorescence intensity was collected at 600 V. CD spectra for the **(E)** far-UV, and **(F)** near-UV/Vis regions for MurB (5 and 20 μM, respectively, black lines) and His_6MurB (2.5 and 10 μM, respectively, violet lines). Emission and CD spectra were recorded in 10 mM KPi, pH 8.0, at 10 °C. (For interpretation of the references to color in this figure legend, the reader is referred to the Web version of this article.)

emissions. Furthermore, the FAD fluorescence within MurB and His_6-MurB was 3.6-fold and 2-fold higher, respectively, than that of free FAD. These observations agree with the fluorescence of free FAD being quenched by its adenine nucleotide that fold over the isoalloxazine, and indicate that FAD is tightly bound in both MurBs in an extended conformation and with an isoalloxazine ring exposed to the solvent (resulting in minimal fluorescence quenching by the protein environment). The far-UV CD spectra of both MurB forms showed minima at 208 and 221 nm, envisaging a high content of α-helixes (Fig. 2E). In both MurB and His_6MurB forms, the near-UV/Vis CD spectra displayed minima at 271, 368, and 460 nm, with additional shoulders at 317 and 494 nm (Fig. 2F).

MurB underwent also reduction of its FAD by the non-physiological electron donor xanthine/XO system, with the phenosafranin two-electron exchanger ($E_{ox/rd}$ = -252 mV, *vs* HNE) being the dye that better equilibrated with FAD reduction. Fig. 3A illustrates the optical changes observed throughout the MurB/dye reductive process. The dependence of the logarithmic oxidized/reduced concentrations of the enzyme *versus* those of the dye showed a slope close to 1. This observation aligned with a two-electron exchange and allowed for the estimation of a mid-point reduction potential, $E_{ox/hq}$, of −260 ± 3 mV (inset Fig. 3A), which is more negative than that of free FAD ($E^{FAD}_{ox/hq}$ = -219 mV [38]). CV also demonstrated the ability of the FAD of MurB to accept electrons from an electrode source, producing a cyclic voltammogram that showed the presence of a redox couple with well-defined oxidation and reduction peaks for the simultaneous exchange of two electrons (Fig. 3B). In these electrochemical experiments either free FAD or MurB were immobilized on the surface of carbon electrodes, and only one redox couple was observed for each with a mid-point potential of −135 and −180 mV (vs NHE), respectively. Given the potential of free FAD [38], the electrochemically determined redox potential of MurB was corrected by taking into account the difference between solution and electrode values for FAD, obtaining for immobilized MurB a corrected value of −264 ± 5 mV, in close agreement with that reported in the in-solution experiment.

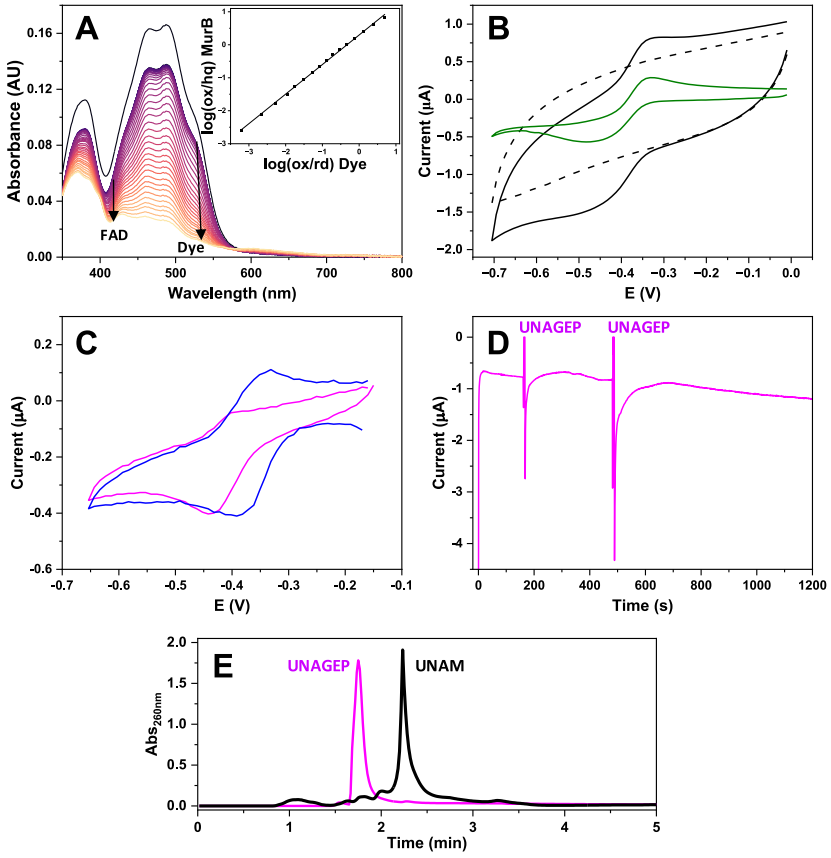

Fig. 3. - Midpoint reduction potential of MurB and its role as an electron transfer mediator to UNAGEP. (A) Spectral evolution upon mid-point reduction potential assessment using phenosafranin as a dye. The black spectrum corresponds to the enzyme before mixing XO, while colored Vis absorption spectra from purple to orange degradation correspond to different time points along protein reduction after adding 200 μL XO to 1000 μL final volume (final concentration 30 nM). Spectra shown were recorded every 5 min for up to 2 h in 50 mM Bis-Tris Propane pH 8.0, 100 mM KCl, 1 mM DTT, at 25 °C. The inset presents the logarithm ratios of oxidized/reduced His_6MurB and oxidized/reduced dye at various time points, as calculated based on absorbance readings taken at 525 nm for the dye and 412 nm for MurB (these specific wavelengths are indicated by black full line arrows in the main figure). **(B)** Cyclic voltammogram of His_6MurB as recorded at 25 °C under anaerobic conditions obtained by applying a potential between 0 and -700 mV with a scan rate of 120 mV/s (black line). The figure shows also the control baseline (dashed black line) and the baseline corrected CV (green). **(C)** CV of His_6MurB co-immobilized on the electrode in the presence of UNAGEP as recorded at 25 °C under anaerobic conditions by applying a potential between −150 and −650 mV with a scan rate of 5 mV/s. First (blue) and second (magenta) scans are shown. **(D)** Chronoamperometry of His_6MurB titrated with two additions of UNAGEP at the time points indicated by an arrow. In B, C and D, the supporting electrolyte was 50 mM KPi pH 7.4, 100 mM KCl, with an Ag/AgCl reference electrode. (E) Overlay of HPLC chromatograms at 260 nm for the UNAGEP substrate of MurB (magenta line) and the product of a CV experiment (black line) in which MurB and UNAGEP were immobilized on the electrode in a 1:5 ratio. (For interpretation of the references to color in this figure legend, the reader is referred to the Web version of this article.)

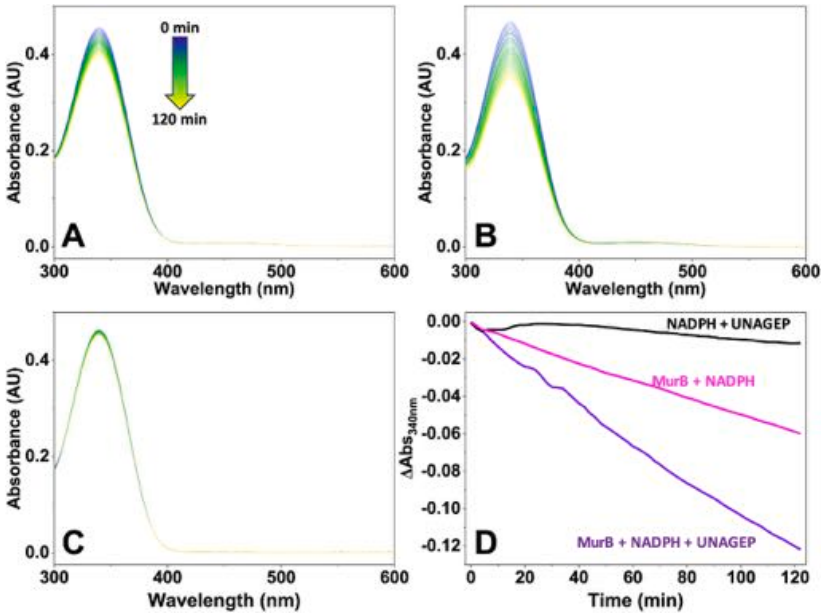

Fig. 4. - Kinetics for the transformation of NADPH into NADP$^+$ by hydride transfer to MurB of *B. ovis*. Spectral evolution for the oxidation of the NADPH (100 μM) by **(A)** MurB (1 μM), **(B)** a MurB-UNAGEP mixture (respectively 1 μM and 5 μM) and **(C)** UNAGEP (5 μM) in the absence of the enzyme. **(D)** Normalized absorbance changes of NADPH at 340 nm for panels (A), (B), and (C). Experiments carried out under aerobic conditions.

3.2. The activity of MurB from B. ovis

MurB enzymes are reported to use NADPH as a reducing power for the reduction of their FAD cofactor to subsequently catalyze the reduction of UNAGEP to UNAM, in a process activated by monovalent cations (Fig. 1). The best conditions for detecting MurB reduction by NADPH were obtained in 50 mM Bis-Tris Propane pH 8.0, 30–100 mM KCl, 1 mM DTT, while minimizing light exposure and employing a relatively high enzyme concentration for a steady-state assay (Fig. 4). Oxidation of NADPH to NADP$^+$ upon hydride transfer to the FAD of MurB was a slow process, with initial velocities normalized to protein concentration ranging from 0.045 to 0.090 min^{-1} over the range of NADPH:MurB ratios (20:1 to 100:1) evaluated. Both, MurB and His$_6$-MurB exhibited similar behavior in the assays when molecular oxygen was used as the potential final MurB electron acceptor. In addition, the previous mixing of MurB with UNAGEP enhanced the MurB activity as followed by its ability to transform NADPH into NADP$^+$ (Fig. 4D).

Time-resolved spectroscopy under anaerobic conditions, using the stopped-flow equipment, was employed to further investigate the kinetics of FAD reduction in MurB by NADPH. Notably, achieving anaerobic conditions in the dark was critical for observing FAD reduction. Fig. 5A–D summarize the spectral evolution during FAD reduction by NADPH. Reduction proceeded as a slow process composed of several phases: an initial absorption decay ($^{app}k_{obs}$ around 6.7 min^{-1}), which accounts for only a small change in absorbance and occurs after a brief lag-phase (Fig. 5B), followed by a second short lag phase that transits into a long linear absorption decay ($^{app}k_{slope,}$ linear slope 522 x 10^{-6} min^{-1}) and is then suddenly followed by the activation of the reduction of the remaining oxidized cofactor ($^{app}k_{obs}$ around 0.22 min^{-1}) (Fig. 5C–D). Pre-incubation of MurB with the second substrate, UNAGEP, significantly impacts the kinetics of MurB reduction by NADPH. As shown in Fig. 5E–G, the addition of UNAGEP nearly eliminates both lag phases and significantly accelerates the initial small decrease in amplitude ($^{app}k_{obs}$ around 25 min^{-1}). However, it has little impact on the later phase, which corresponds to the complete reduction of FAD ($^{app}k_{obs}$ around 0.16 min^{-1}).

To further evaluate the source of the different phases observed during reduction by NADPH, we similarly evaluated the kinetics of the reduction of MurB by non-physiological reductants, namely photoirradiation and sodium dithionite, using also the anaerobic stopped-flow system. Prolonged photoirradiation of MurB by the instrument lamp achieved the slow reduction of FAD to the hydroquinone state ($^{app}k_{obs}$ around 6.0 x 10^{-2} min^{-1}), without traces of semiquinone, after a very long lag phase (Fig. 5H). Notably, this reduction resembles that observed by NADPH when evaluating at long reaction times (Fig. 5D). Reduction of MurB to the FAD hydroquinone state upon mixing with sodium dithionite resulted in a faster process ($^{app}k_{obs}$ of 630 min^{-1}) with no traces of semiquinone being detected (Fig. 5I), but also after a short lag period (0.2 s) before bleaching of the FAD band started.

CV was used to explore whether electrochemically reduced MurB was able to reduce the UNAGEP substrate. As shown in Fig. 3C, co-immobilization of MurB with UNAGEP on the electrode produced notable changes in the CV signal, shifting the peak corresponding to the reductive flavin process towards lower potentials, while considerably decreasing the flavin peak in the oxidative process. These features indicate that UNAGEP binds close to the flavin isoalloxazine, and suggest that electrons pass from reduced FAD in MurB to UNAGEP. To further support the second fact, chronoamperometry of MurB at the fixed potential of −700 mV was evaluated, showing increase in the current upon two consecutive additions of UNAGEP (Fig. 3D). This feature further supports reduction of UNAGEP by electrochemically reduced MurB. Furthermore, HPLC analysis of the products of CV and chronoamperometry experiments with MurB and UNAGEP confirmed the disappearance of UNAGEP in favor of the appearance of a new and single peak, which considering the properties of the enzyme and UNAGEP substrate, must be the UNAM product (Fig. 3E). This UNAM peak was also detected when the MurB FAD was reduced by dithionite or light in the presence of UNAGEP (not shown). In these cases, additional peaks appeared in the chromatogram, likely resulting from damage to the substrates or products caused by these treatments.

3.3. Impact of ligands in the thermal stability of MurB

To detect binding of ligands to MurB we first evaluated the potential ability of the NADP$^+$ product to disturb the spectroscopic properties of FAD when the nicotinamide of the cofactor comes into close proximity to the isoalloxazine by using difference spectroscopy. No spectroscopic change consistent with this potential competent binding at the active

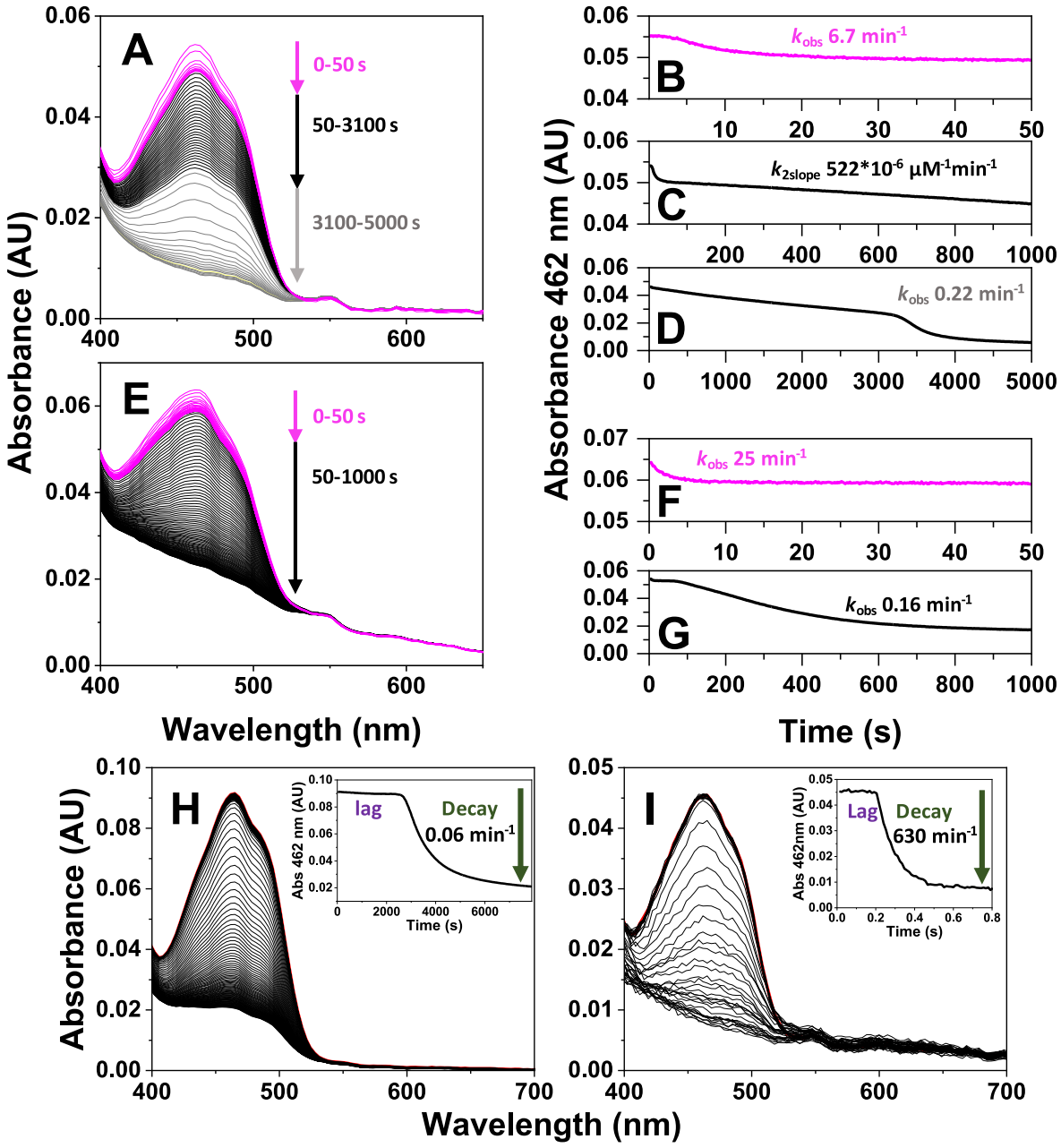

Fig. 5. - Kinetics for the reduction of the cofactor FAD of MurB of *B. ovis*. **(A)** FAD spectral evolution in the 400–700 nm region during the reduction of MurB (~8 µM, final concentration) by mixing with NADPH (100 µM) in the stopped-flow system. Spectra are shown at different times in the 0–5000 s range after mixing. Evolution of absorbance decay at 462 nm as measured along total times of **(C)** 50 s, **(D)** 1000 s and **(E)** 5000 s. **(E)** Evolution of spectral features for the FAD cofactor in the 400–700 nm range during the reduction of MurB previously incubated with UNAGEP (~8 µM and 100 µM respectively) by mixing with NADPH (100 µM) in the stopped-flow system. Spectra are shown at different times in the 0–1000 s range after mixing. Evolution of absorbance decay at 462 nm as measured in total times of **(F)** 50 s and **(G)** 1000 s. All measurements were conducted in 50 mM Bis-Tris Propane pH 8.0, 100 mM KCl, 1 mM DTT, under anaerobic conditions (obtained in the strict dark) at 25 °C. **(H)** Spectral evolution for the photoreduction of MurB (~10 µM, final concentration) upon photoirradiation by the stopped-flow detection light in the 400–700 nm region, in 50 mM Bis-Tris Propane pH 8.0, 100 mM KCl, 1 mM DTT, 20 % glycerol, and 50 mM EDTA at 25 °C. Spectra are shown at different times in the 0–8000 s range after mixing the protein with an equal volume of buffer in the reaction chamber. **(I)** Spectral evolution of MurB (~5 µM, final concentration) upon fast mixing with sodium dithionite (150 µM) in 50 mM Bis-Tris Propane pH 8.0, 100 mM KCl, 1 mM DTT at 25 °C. Spectra are shown at different times in the 0–2 s range after mixing. In (H) and (I) the insets show the time dependent absorbance evolution at 462 nm.

site was detected.

As an alternative to evaluate the binding of substrates/products or analogs to the enzyme, even far from the isoalloxazine, we evaluated their impact on MurB stability by monitoring its thermal unfolding through changes in far-UV CD, as well as in tryptophan and flavin fluorescence (Fig. 6). In general, global analysis of data indicated that MurB and His_6MurB suffer complex thermal denaturation processes with formation of intermediate species. In their substrate-free states MurB data best fit to a four-state unfolding process (N↔I_1↔I_2↔U), while for His_6MurB a three-state unfolding process (N↔I↔U) explains the experimental data (Table 1). The three T_m values characterizing the MurB unfolding are lower than the two characterizing the His_6MurB unfolding (Fig. 6A–B, Table 1). The contributions of secondary structure unfolding, as well as tryptophan or FAD exposure to the solvent to the process also differed between the two MurB forms for each transition.

The presence of the substrates NADPH/UNAGEP or its precursor,

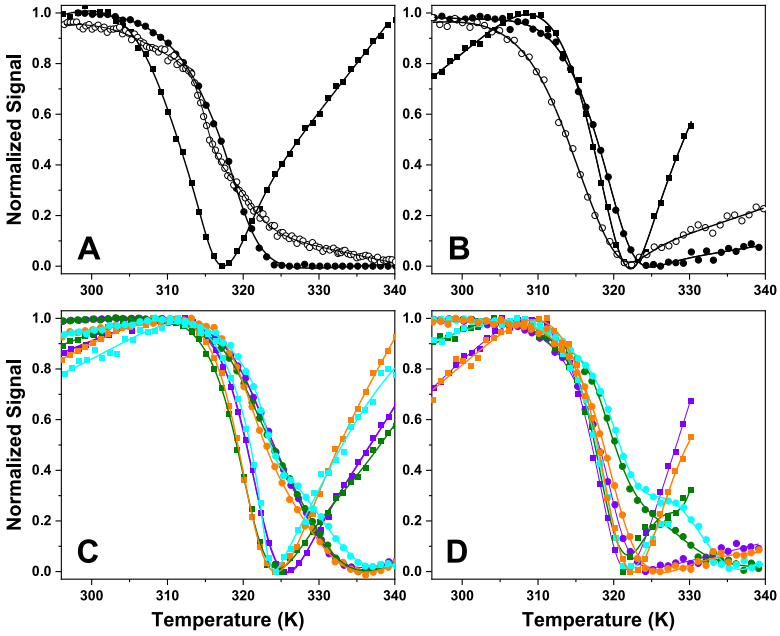

Fig. 6. - Impact of ligands on the thermal stability of MurB of *B. ovis*. Thermal unfolding curves for **(A)** MurB and **(B)** His_6MurB. Unfolding was monitored by changes in far-UV CD (222 nm, open circles), tryptophan fluorescence (λ_{ex} = 280 nm and λ_{em} = 330 nm, closed squares) and FAD fluorescence (λ_{ex} = 460 nm and λ_{em} = 527 nm, closed circles) signals. Thermal unfolding curves for **(C)** MurB and **(D)** His_6MurB in the presence of $NADP^+$, UNAGEP, UNAGEP + $NADP^+$ and UNAG, respectively shown in violet, green, cyan and orange (symbols as in (A) and (B)). For clarity in (C) and (D) only tryptophan and FAD fluorescence curves are shown. Curves were recorded in 10 mM KPi, pH 8.0 from 290 to 350 K, and are shown roughly normalized from 1 to 0 with global fits for each condition shown in continuous lines. Protein concentrations were 5 μM for far-UV CD, and 10 μM for fluorescence. UNAG and UNAGEP concentrations were in 10-fold excess regarding MurB, and $NADP^+$ was in 20-fold excess. (For interpretation of the references to color in this figure legend, the reader is referred to the Web version of this article.)

Table 1
Impact of ligands on the thermal stability parameters for MurB and His_6MurB. Values obtained by global fitting of far-UV CD thermal denaturation curves, together with those followed by tryptophan and FAD fluorescence. Data obtained in 10 mM KPi pH 8.0. (n = 3, error on T_m values is ±2 and in ΔH<20 % of the value).

Sample	Ligand	T_{m1} (K)	ΔH_1 (kcal/mol)	T_{m2} (K)	ΔH_2 (kcal/mol)	T_{m3} (K)	ΔH_3 (kcal/mol)	Fitted Mechanism	ΔT_{m1} (K)	ΔT_{m2} (K)	ΔT_{m3} (K)
MurB	–	309	53	315	175	318	104	$N \rightarrow I_1 \rightarrow I_2 \rightarrow D$	–	–	–
	$NADP^+$	312	82	322	96	328	74	$N \rightarrow I_1 \rightarrow I_2 \rightarrow D$	3	7	10
	NADPH	309	51	320	85	328	93	$N \rightarrow I_1 \rightarrow I_2 \rightarrow D$	1	5	10
	UNAGEP	315	68	321	93	328	68	$N \rightarrow I_1 \rightarrow I_2 \rightarrow U$	6	6	10
	UNAGEP + $NADP^+$	320	50	323	316	331	55	$N \rightarrow I_1 \rightarrow I_2 \rightarrow U$	11	8	13
	UNAG	313	53	321	91	327	53	$N \rightarrow I_1 \rightarrow I_2 \rightarrow U$	4	7	9
His_6MurB	–	314	53	322	120			$N \rightarrow I \rightarrow U$	–	–	–
	$NADP^+$	318	81	320	154			$N \rightarrow I \rightarrow U$	4	−2	
	NADPH	315	61	319	77			$N \rightarrow I \rightarrow D$	1	−3	
	UNAGEP	314	80	318	91	329	105	$N \rightarrow I_1 \rightarrow I_2 \rightarrow U$	0	−4	7[a]
	UNAGEP + $NADP^+$	316	101	321	82	326	44	$N \rightarrow I_1 \rightarrow I_2 \rightarrow U$	2	−1	4[a]
	UNAG	315	80	318	80	320	60	$N \rightarrow I_1 \rightarrow I_2 \rightarrow U$	1	−4	−2[a]

[a] This ΔT corresponds to T_{m3} in the presence of ligand minus T_{m2} in its absence.

UNAG (lacking the redox active enolpyruvyl moiety), or the $NADP^+$ product increased the T_m values for MurB thermal unfolding (Fig. 6C–Table 1). These temperatures further increased when simultaneously incubating with $NADP^+$ and UNAGEP. The presence of either UNAGEP or UNAG induced the appearance of an additional state during His_6MurB unfolding, while $NADP^+$/H did not alter the three-state unfolding process (Fig. 6D–Table 1). UNAGEP or UNAGEP + $NADP^+$ also differently impacted T_m values: changes in T_{m1} hardly envisaged stabilization by ligands; the small changes in T_{m2} suggested slight destabilization of the second intermediate state; and changes in T_{m3} suggested stabilization of some molecules of His_6MurB versus total unfolding. Noticeably, the mixing of UNAG with His_6MurB did not promote any stabilization, but contributed to a slight earlier unfolding. Notably, FAD fluorescence was the primary contributor to T_{m3} across all MurB forms and substrate conditions, while tryptophan fluorescence contributed most significantly to T_{m1}. Altogether these data indicate that ligand binding has a moderate impact on protein stability.

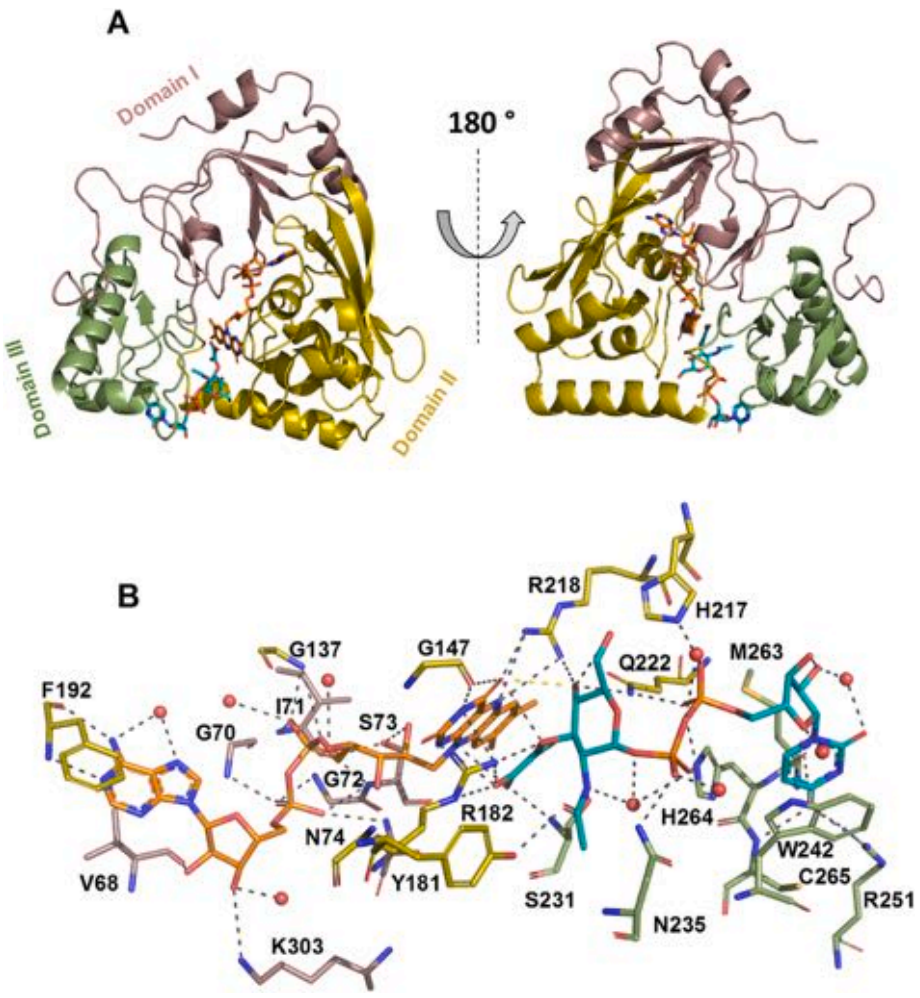

Fig. 7. - Structural features of the crystal $MurB_{ox}$:UNAGEP complex of *B. ovis*. (A) Overall structure (two views related by 180° rotation) with the FAD cofactor and the UNAGEP substrate shown as sticks with C atoms in orange and teal respectively. Domains I, II and III are colored in dark salmon, olive and smudge, respectively. **(B)** Detail of the FAD and UNAGEP binding sites. Residues involved in H-bonds (dotted grey lines) are colored by domain. Water molecules are represented as red spheres. (For interpretation of the references to color in this figure legend, the reader is referred to the Web version of this article.)

3.4. The $MurB_{ox}$:UNAGEP crystal structure

The structure of MurB from *B. ovis* is here solved in its oxidized state in complex with UNAGEP, $MurB_{ox}$:UNAGEP. Like other MurB structures, it folds into three distinct domains (Fig. 7A and **SP2**, **Table SP1**). Domain I (residues 1–88 and residues 301–322) consists of three α-helices and six β-strands, which form a four-stranded mixed β-sheet and a two-stranded parallel β-sheet. Domain II (residues 89–225) is made of a five-stranded antiparallel β-sheet and six α-helices. Both domains, I and II, create the binding site for the FAD cofactor. On the other hand, domain III (residues 226–300) folds into a three-stranded antiparallel β-sheet and two α-helices and, together with domain II, contribute to the binding of the UNAGEP substrate (Fig. 7). Noticeably, MurB from *B. ovis* is the only one out of the Type II crystal structures having a 12–16 amino acids extension at the C-terminus, due to its longer sequence (Figures SP2B-D). These residues make a loop that runs parallel to the C-terminal α-helix (residues 276–293), being stabilized by a H-bond between the N atom of F317 at the C-terminal loop and the OE1 atom of E284 in the helix (**Figure SP2E**).

The FAD binds in an extended conformation, similarly to other MurBs, and is stabilized by a network of H-bonds with two arginine residues (R182 and R218) situated in close proximity to the isoalloxazine (Fig. 7B, SP3A, Table SP3). The UNAGEP substrate is bound in a competent orientation for HT with respect to the FAD isoalloxazine (Fig. 7B and **SP3B**), since its enolpyruvyl moiety's C3 atom is positioned 3.2 Å from the N5 of the FAD that serves as the hydride source (Tables SP3 and SP4). R182 (domain II) and S231 (domain III) sit in close nearby of the enolpyruvyl of UNAGEP. This envisages for them some role in the HT mechanism: R182 might stabilize the transient carbanion expected at C2 of the enolpyruvate, while S231, whose hydroxyl is 3.1 Å away from C2, might act as proton donor to quench this carbanion when the D-lactyl ether product is formed.

3.5. Dynamics in complexes of MurB with substrates

To further characterize the interaction and dynamic properties of both NADPH and UNAGEP, structural models of MurB free and in complex with substrates were investigated by MD simulations. Models were produced for the $MurB_{hq}$:UNAGEP as well as for the $MurB_{ox}$:NADPH and $MurB_{ox}$:NADPH:UNAGEP complexes. Thus, all generated models would correspond to those for the reactants for the flavin reductive and oxidative half-reactions. Simulations hardly showed changes in the gyration radius and equilibrated average Cα RMSD fluctuations of 1.8 ± 0.3, 1.2 ± 0.1, 1.5 ± 0.3 and 1.5 ± 0.3 Å, respectively, for free $MurB_{ox}$, $MurB_{hq}$:UNAGEP, $MurB_{ox}$:NADPH and $MurB_{ox}$:NADPH:UNAGEP), suggesting overall equilibrium reached by all systems.

Domain III was identified as the most flexible in free $MurB_{ox}$, being

the one contributing mostly to substrate binding (Figure SP4A). Loops making the N- and C-terminals, both at domain I, also showed high mobility. Regions of domains I and II binding to the adenine, pyrophosphate and ribityl moieties of FAD were the ones exhibiting lower flexibility (Figure SP5A). Binding of either NADPH or UNAGEP slightly reduced the mobility of domain III, while simultaneous binding of both substrates exhibited an intermediate behavior (Figures SP4 and SP5). The C-terminal of α helix 213–225 in domain II and the loop/α helix 234–247 in domain III are also relatively flexible. These regions are at the entrance of the substrates binding cavity and therefore allocate the non-reactive moieties of NADPH and UNAGEP. Noticeably, the simultaneous incorporation of the two ligands into the system did not induce a significant increase in the isoalloxazine ring environment mobility, and the reactive moieties of both substrates were allocated in the cavity. Nonetheless, the stacking of the reactive nicotinamide of NADPH on the FAD isoalloxazine was favored over that of the enolpyruvate of UNAGEP (Figs. 8 and 9), in agreement with the expected sequential reaction mechanism.

FAD showed very low mobility of its ribityl, pyrophosphate and, particularly, adenine moieties. Consistent with this observation, the protein regions making their environment (overall domain I) exhibited very little fluctuation thus maintaining the protein-FAD interaction pattern (Figure SP5-SP7). Moreover, in both, $MurB_{ox}$ and $MurB_{ox}$:NADPH, main interactions between the isoalloxazine and the protein were preserved; namely O2, N3 and O4 of the isoalloxazine being stabilized by side chains of R182 and, particularly, R218 (Fig. 10A–B and **SP7A-B)**. However, UNAGEP disturbed the interactions between the isoalloxazine and domain II upon MD energetic optimization. Of notice are the new interactions established by Q222 with the N5 and O4 of the isoalloxazine, while interactions of O2 and N3 with the 146–147 residues are replaced by those with the side chain of R182 (Fig. 10C and **SP7C)**.

In both $MurB_{ox}$:NADPH and $MurB_{ox}$:NADPH:UNAGEP the nicotinamide was considerably less flexible than the pyrophosphate and adenine nucleotide portions (Figures SP6B-D). These latter moieties sit at the entrance of the binding cavity, are highly exposed to the solvent and establish sporadic contacts with residues from domains III (N235) and II (N145 and H217). On the contrary, the nicotinamide nucleotide moiety maintains a more stable position, providing in all models, equivalent environments and competent contacts between the nicotinamide and the isoalloxazine for HT from the C4 of the reduced nicotinamide to the N5 of oxidized isoalloxazine (Figs. 8, 9C and 10). Beyond the reacting atoms, close contacts between O2 and N3 of the isoalloxazine and N7N of the NADPH suggest that they contribute to the reaction environment. In addition, in general, S231, the catalytic residue, remains close to the nicotinamide (Fig. 10B and SP8). Evaluation of UNAGEP in the $MurB_{hq}$:UNAGEP model showed the coupling of both the N5 of the FAD_{hq} isoalloxazine and the side-chain of S231 with the reactive enolpyruvate group of UNAGEP as highly populated (Fig. 9A–B and 10C). This envisage competent relationships for catalysis that match with the crystal structure of $MurB_{ox}$:UNAGEP (Fig. 7). Nonetheless, within the active site cavity the enolpyruvyl of UNAGEP exhibits larger mobility than the nicotinamide of NADPH (**Figure SP6**).

3.6. Sequence analysis and phylogeny of MurB in Brucella spp. and other bacterial species

To evaluate the representativeness of MurB of *B. ovis* within its genus, 52 protein sequences from *Brucella* species (**Table SP5**) were compared. MurB of *B. endophytica* showed the lowest identity (82 %) with regard to the *B. ovis* protein, while for the others identity ranged from 90 to over 99 % (**Figure SP10**). All MurBs from *Brucella* lack the typical Tyr-loop of Type I and preserve the catalytic serine of Type IIa. The phylogenetic analysis of MurBs from *Brucella* revealed their distribution into three major clades separated by short branches (Fig. 11A), what indicates high structural similarity and minor divergences at the active site. The study further examined 80 MurB sequences from 74 different bacteria (certain organisms exhibited two MurB isoforms), including representatives from the ESKAPE group, as well as other human and animal pathogens (**Table SP6**). MSA leads to their classification into Types I and II, based on the presence of the Tyr-loop in the first case (**Figure SP11**). Notably, the *A. phagocytophilum* sequence displayed a tyrosine residue at the position expected for the catalytic serine or cysteine. MurB homologues from *B. quintana*, *B. schoenbuchensis*, and *S. meliloti* exhibited the highest sequence identity (76 %) to MurB from *B. ovis* within Type IIa, with other sequences showing identities ranging from 71 to 48 %. A considerable number of conserved residues groups in motifs that are involved in substrates and cofactor binding (**Figure SP12**). Motifs corresponding to FAD binding showed specific sequences for different MurB Types (**Table SP7**) and amino acids contributing to UNAGEP or NADPH binding (including N149, Y181, R182, R218, Q222, V224, N235, W242, S244, R251, H264, C265 and E301, *B. ovis* numbering) are in general highly conserved or represent conservative substitutions in Type II MurBs. Some of them are also conserved in enzymes of Type I, and, again, the motifs containing them slightly differ depending on the MurB Type. A gene with a unique ORF that encoded a fused MurB/C protein was also identified in some *Verrucomicrobia* and *Methylacidiphilales* during the search [72]. The phylogenetic analysis of the selected MurB sequences revealed a distribution into four major distinct clades (Fig. 11B). The MurB Type I cluster is the most divergent clade, with a bootstrap value > 98. MurB Type II is distributed in three clades, highlighted in blue (Type IIa) and green (Type IIb) with bootstrap values > 92. All MurB Type IIa analyzed (47) cluster together but distribute in two subgroups. One of them, the most divergent, contains sequences of α-proteobacteria. MurBs of Type IIb separate in two groups, with the most divergent including gram-negative and gram-positive bacteria isolated from soil and marine sediments involved in the methane and nitrogen cycles, and legume–microbiome interactions. The other subgroup clusters within the clade of MurB Type IIa, and includes sequences of a variety of species from diverse families.

4. Discussion

4.1. Recombinant MurB from B. ovis catalyzes a slow oxidation of NADPH

The MurB enzyme from *B. ovis* and its His_6-tagged variant were successfully purified to homogeneity, as well as folded and incorporating the FAD cofactor similarly (Fig. 2). Both forms exhibited high solvent accessibility of their isoalloxazine rings, with the His_6-tag slightly increasing the fluorescence quenching of both tryptophan and FAD. Structural models, including those generated by AlphaFold 3 (https://alphafoldserver.com/), showed no significant differences in folding between MurB and His_6MurB, though a segment of the His_6-tag (residues 12–23, particularly F17) interacted with W34, whose side-chain is solvent-exposed and directly in contact with the FAD isoalloxazine, as well as with domain III (Fig. 7B). This interaction may explain the differences in fluorescence quenching (Fig. 2C–D), thermal stabilization (Fig. 6), and activity in the presence of certain ligands like UNAGEP (Figs. 4–5). Thermal unfolding experiments confirmed the binding of NADPH, $NADP^+$, and UNAGEP, and suggested that $NADP^+$ and UNAGEP could bind simultaneously (a feature also envisaged by MD simulations (Fig. 8C and 9C)). These findings also indicated that domain III of MurB, involved in substrate binding, may be more susceptible to thermal denaturation than domains interacting with FAD.

MurB from *B. ovis* catalyzes a two-electron exchange with a midpoint potential comparable to that reported for *E. coli* MurB ($E_{ox/hq} = -234$ mV). It accepts a hydride from NADPH slowly, a process enhanced in the presence of UNAGEP, which also acts as an electron acceptor to produce UNAM when MurB is reduced either by NADPH, light or electrochemically (Figs. 3 and 4). Fast kinetic analyses under anaerobic conditions

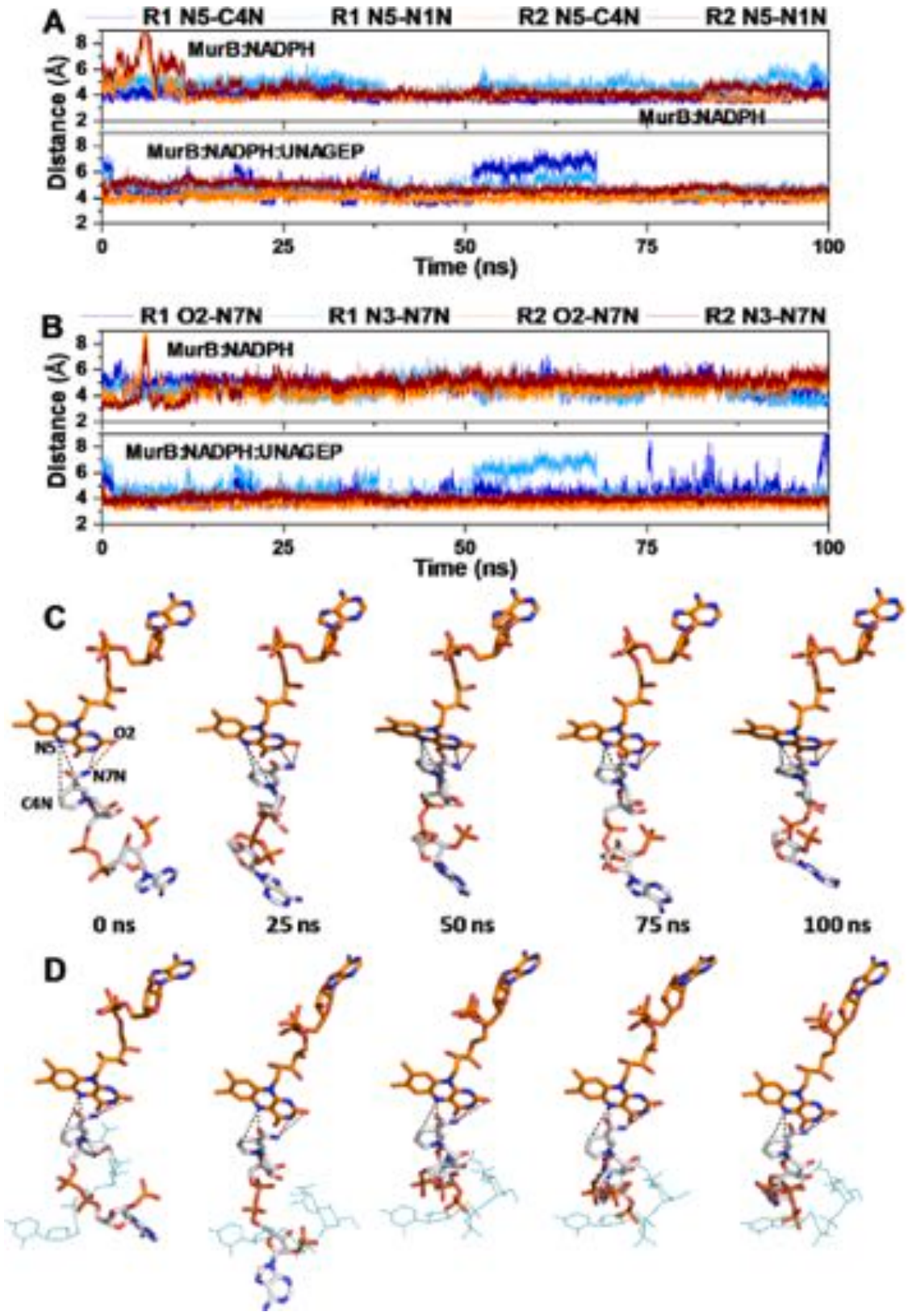

Fig. 8. - Organization of the active site in complexes of $MurB_{ox}$ with NADPH along the MD simulations. Evolution of distances between **(A)** N5 of the isoalloxazine and C4N and N1N of the nicotinamide, and **(B)** N7N of the nicotinamide and O2 and N3 of the isoalloxazine. Top and bottom panels respectively correspond to the MD simulations for $MurB_{ox}$:NADPH and $MurB_{ox}$:NADPH:UNAGEP models. All panels show data for replicates 1 and 2 (R1 and R2), respectively colored in blue and brown degradations. Structural dynamics of the isoalloxazine-nicotinamide coupling along the MD simulations in **(C)** $MurB_{ox}$:NADPH and **(D)** $MurB_{ox}$:NADPH:UNAGEP. Snapshots are shown at 0, 25, 50, 75 and 100 ns along the MD simulations of R2 (taken as representative). FAD and NADPH are shown in CPK colored sticks with carbons respectively in orange and grey. When present, UNAGEP is shown in teal lines. (For interpretation of the references to color in this figure legend, the reader is referred to the Web version of this article.)

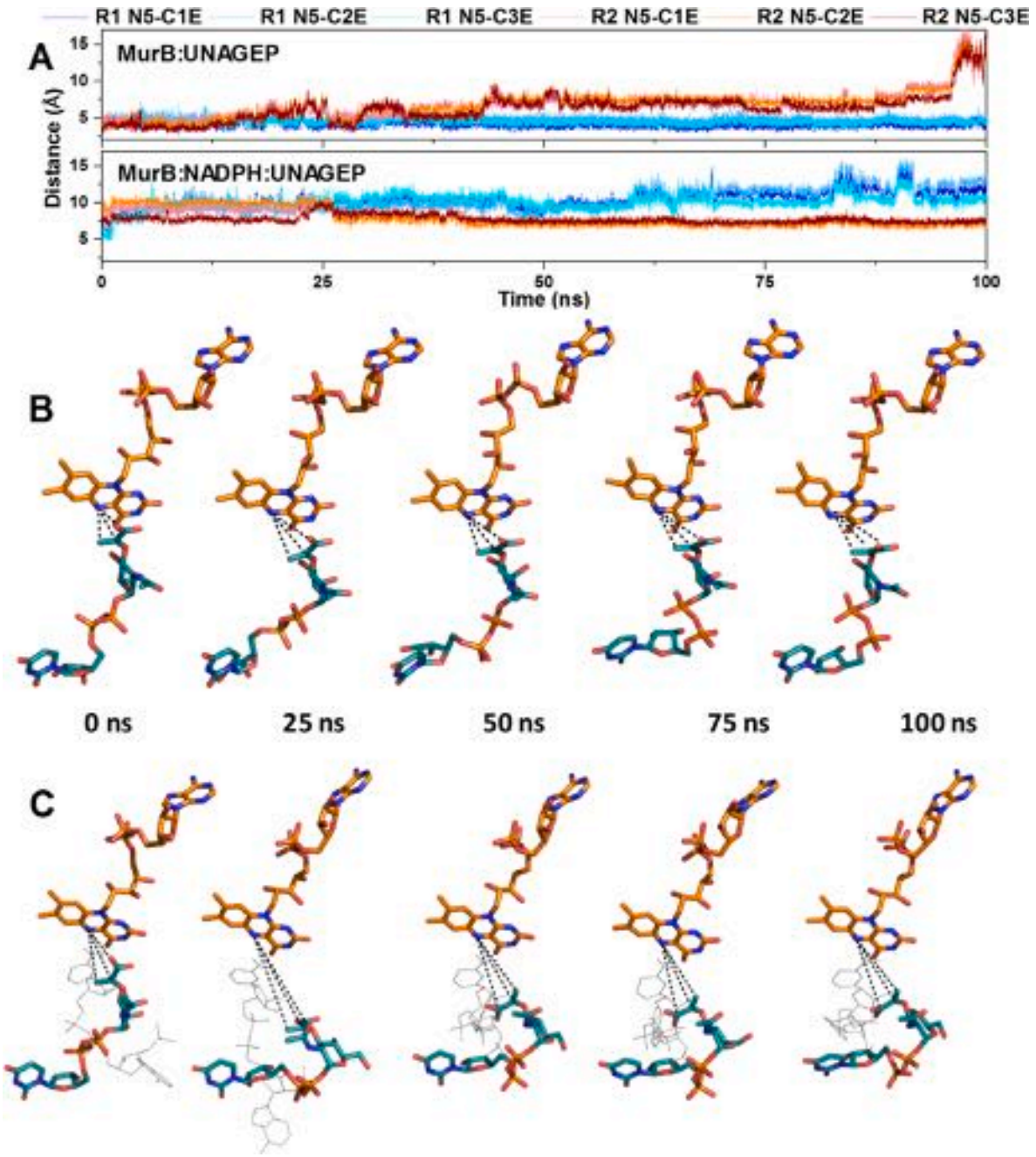

Fig. 9. - Organization of the active site in complexes of MurB with UNAGEP along the MD simulations. (A) Evolution of distances between N5 of the isoalloxazine and C1E, C2E and C3E of UNAGEP. Top and bottom panels respectively correspond to the MD simulations for the $MurB_{hq}$:UNAGEP and $MurB_{ox}$:NADPH:UNAGEP models. In all panels data for replicates 1 and 2 (R1 and R2) are respectively colored in blue and brown degradations. Structural dynamics of the enolpyruvyl-isoalloxazine coupling along the MD simulations in **(B)** R1 of $MurB_{hq}$:UNAGEP and **(C)** R2 of $MurB_{ox}$:NADPH:UNAGEP. Snapshots are shown at 0, 25, 50, 75 and 100 ns along the MD simulations. FAD and UNAGEP are shown in CPK colored sticks with carbons respectively in orange and teal. When present, NADPH is shown in grey lines. (For interpretation of the references to color in this figure legend, the reader is referred to the Web version of this article.)

reveal lag phases before FAD reduction (Fig. 5), potentially due to residual oxygen reoxidizing reduced MurB. However, given low oxygen levels, MurB's non-oxidase nature, and the high reductant concentration, oxygen alone is unlikely the cause. An alternative hypothesis attributes the lag phases to conformational rearrangements at MurB's active site, facilitating FAD reduction [73]. This is here supported by shorter lag phases and reduced initial absorption decay when UNAGEP is present, indicating that this substrate influences nicotinamide moiety accommodation, as well as by absorption decay occurring in two distinguishable steps: an initial minimal decay likely linked to NADPH accommodation and a subsequent major decay corresponding to FAD reduction (Fig. 5). MD simulations presented in this manuscript suggest that both substrates may interact with the enzyme simultaneously, increasing the overall protein-ligand flexibility. This highlights the potential importance of UNAGEP-induced conformational changes in enhancing the MurB's catalytic efficiency.

It is noteworthy that kinetic parameters for MurBs have only been reported from three species so far (**Table SP8**): MurB Type I from *E. coli* (gram-negative) [5,8,10,13], and MurBs of Type IIa from *S. pneumoniae* [11] and *S. aureus* [28]. Given the potential of MurB as an antimicrobial target and the fact that the PDB contains nearly 20 structures from at least 8 distinct species (**Table SP1**), the number of enzymes kinetically

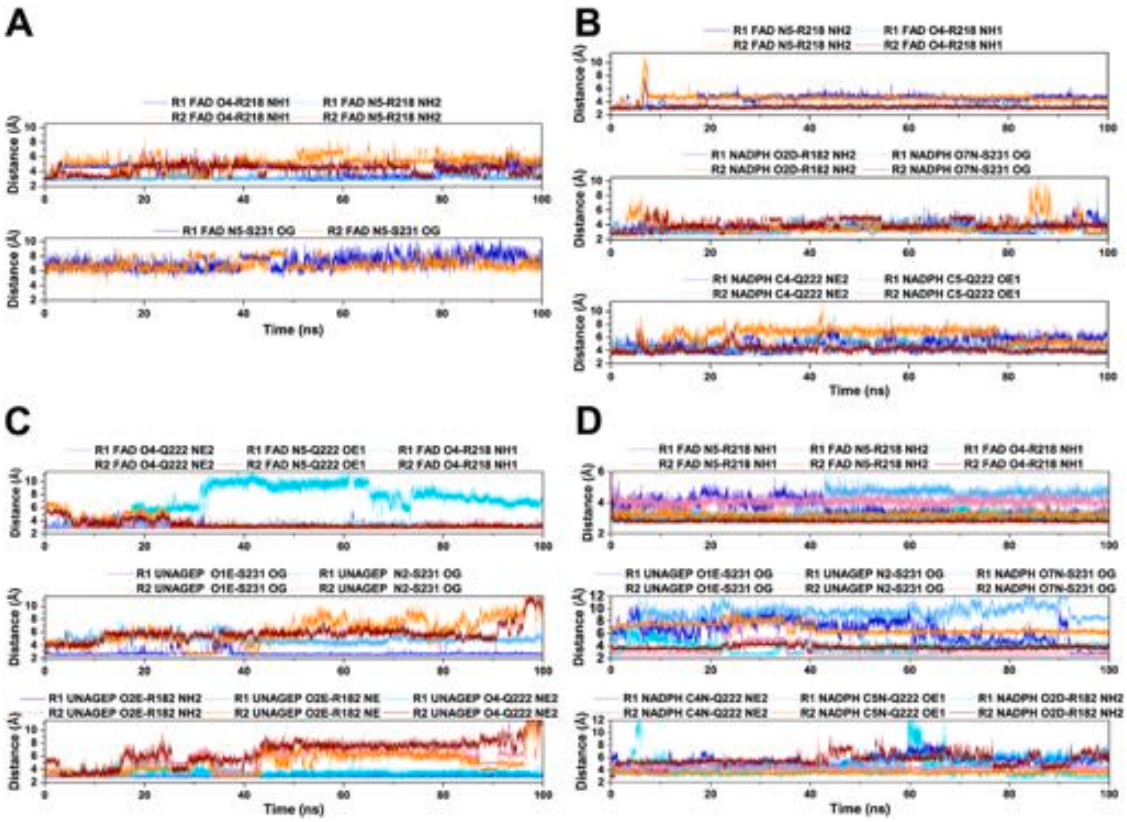

Fig. 10. - Trajectories for the interaction of residues at the active and ligand binding sites of MurB with reactive moieties of FAD, NADPH and UNAGEP in the 100 ns MD simulations. Data are shown for **(A)** free $MurB_{ox}$, **(B)** $MurB_{ox}$:NADPH, **(C)** $MurB_{hq}$:UNAGEP and **(D)** $MurB_{ox}$:NADPH:UNAGEP. All panels show data for replicates 1 and 2 (R1 and R2) colored in blue and brown degradations, respectively. (For interpretation of the references to color in this figure legend, the reader is referred to the Web version of this article.)

characterized appears low. Additionally, reported kinetic parameters exhibit significant heterogeneity in k_{cat} and K_m values, and as a consequence in catalytic efficiency (**Table SP8**), as well as by substrates producing important inhibition effects [7]. Thus, the values reported for MurB of *E. coli* range from 900 to 2700 min^{-1}, 11 to 100 $\mu M^{-1}min^{-1}$, and 72 to 1160 $\mu M^{-1}min^{-1}$ respectively for k_{cat}, K_m^{NADPH} and K_m^{UNAGEP}. For MurB of *S. aureus,* the corresponding values are 270–474 min^{-1}, 73 $\mu M^{-1}min^{-1}$ and 15 to 41 $\mu M^{-1}min^{-1}$, while the values reported for *S. pneumoniae* are 800–1080 min^{-1}, 53-79 $\mu M^{-1}min^{-1}$ and 89 $\mu M^{-1}min^{-1}$. These features could also relate with some of these enzymes exhibiting low turnover numbers. Moreover, the observed low reaction velocity of MurB from *B. ovis* may be associated with the bacterium's slow growth rate, a characteristic adaptation of intracellular pathogens. This contrasts with the higher growth rates observed in bacteria such as *E. coli*, *S. aureus* and *S. pneumoniae*. Future studies aimed at determining steady-state kinetic parameters and potential inhibition constants for substrates during the catalytic cycle of MurB from *B. ovis* will be surely of help to the understanding of its mechanism.

4.2. The crystal structure of the $MurB_{ox}$:UNAGEP complex reveals a catalytically competent organization

Structural comparisons of the crystal *B. ovis* $MurB_{ox}$:UNAGEP complex (Fig. 7) with Type I MurBs (**Table SP1** and **Figure SP2A**) show RMSD values ranging from 1.26 to 2.62 Å (based on 195 to 201 Cα atoms). MurB of *B.ovis* features an additional N-terminal tail of 20–25 residues forming an extra α-helix. Additionally, it lacks two regions critical to Type I MurBs: the Tyr-loop (residues 189/204 to 212/225 in enzymes of *P. aeruginosa/E. coli*, respectively) that includes a conserved Tyr (Y196/210) involved in UNAGEP interaction and regulating access to the active site (**Figure SP2A**) [8], and the βαββ fragment on the opposite side of the substrate access channel [9,24,26]. When compared with Type IIa (the group it belongs to) it yielded RMSD values from 0.87 to 1.14 Å (Figures SP2B-D). It also aligns well with Type IIb MurB from *T. caldophilus* (RMSD 0.98 Å for 181 aligned Cα atoms), which features a catalytic cysteine (C198) rather than the serine (S231 in *B. ovis*) typical in Type IIa enzymes.

Residues at the active site of MurB interacting with UNAGEP align with previously proposed roles for equivalent residues in the $MurB_{ox}$:UNAGEP complex of *E. coli* [8,9]. Structural comparisons with Type I (MurB of *E. coli*, 2BMR) and Type IIb (MurB of *T. caldophilus,* 2GQU) show that the UNAGEP's enolpyruvyl motif consistently faces the FAD isoalloxazine in a conserved orientation (**Figure SP2F**). However, the UDP moiety differs in position, constrained in MurB of *E. coli* by two H-bonds between the hydroxyl of Y190 and the O1A/O3A atoms of UNAGEP. This interaction is absent in Type II MurBs, which lack the Tyr-loop. Despite these differences, structures of MurBs, with or without UNAGEP, are highly similar, and the residues forming the active site and mediating H-bonds with FAD and UNAGEP are highly conserved across species (Figures SP11-12). Exceptions include variable positions such as H217 and M263 that are respectively situated near the conserved R218 and within the ^{258}AxxSxxHx(N/G)F^{267} motif (*B. ovis* numbering), reflecting subtle species-specific adaptations.

4.3. Theoretical models envisage competent binding for catalysis of NADPH to $MurB_{ox}$ of B. ovis

Theoretical energetically optimized models for the $MurB_{ox}$:NADPH reactant complex from *B. ovis* suggest that the nicotinamide portion of NADPH is stably positioned within the active site, with its C4 hydride donor atom optimally aligned for transfer to the N5 acceptor on the isoalloxazine ring (Figs. 8 and 10). In contrast, the adenine nucleotide

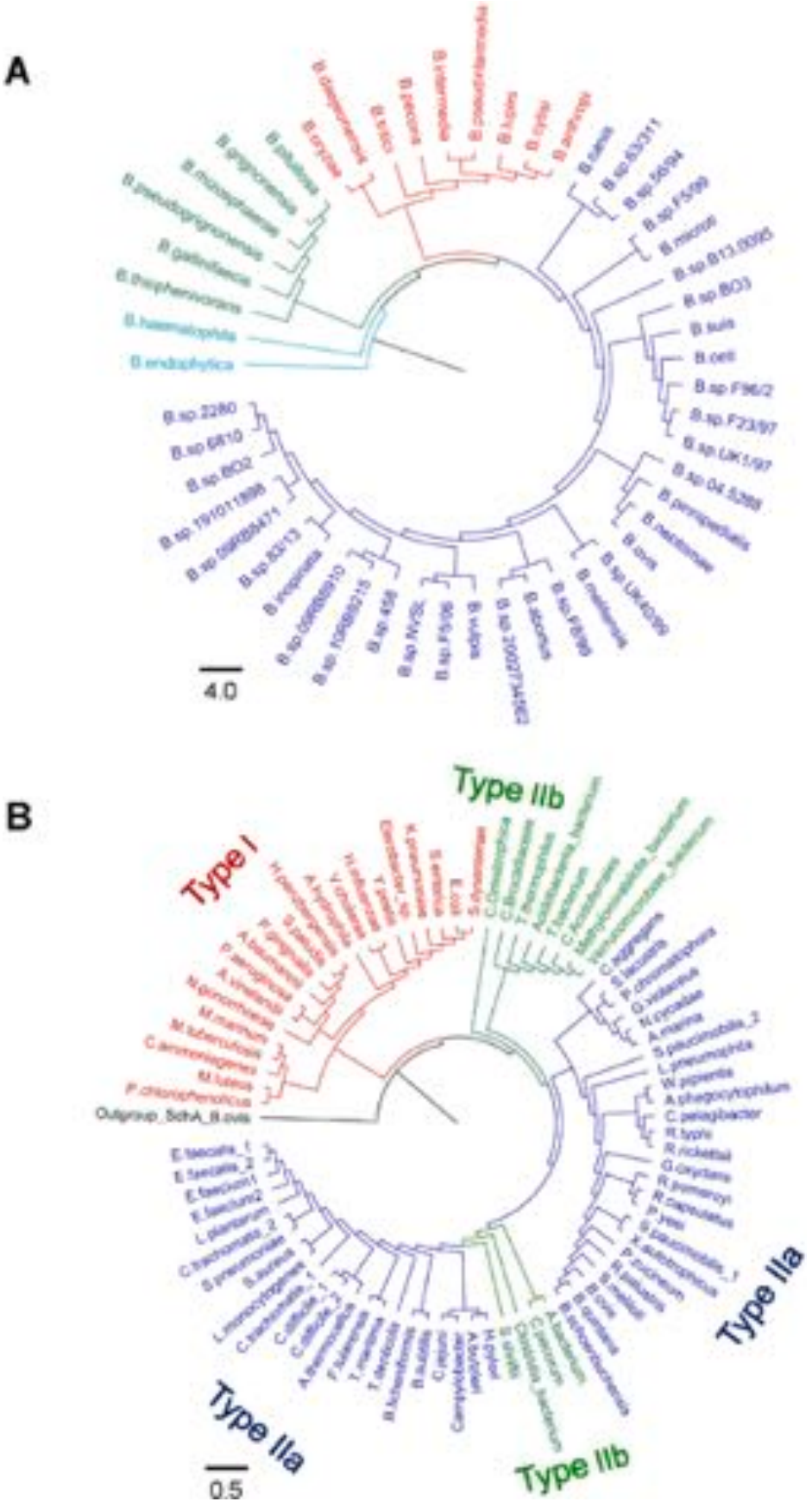

(caption on next page)

Fig. 11. - Phylogeny of MurB. (A) Phylogenetic cladogram of 51 *Brucella* species. Clade 1 comprised the sequences of *B. thiophenivorans, B. gallinifaecis, B. pseudogrignonensis, B. rhizosphaerae, B. grignonensis* and *B. pituitosa* with a bootstrap value of 95. Clade 2 includes sequences from *B. oryzeae, B. daejeonensis*, *B. tritici*, *B. pecoris*, *B. intermedia*, *B. peseudintermedia*, *B. lupini*, *B. cytisi* and *B. anthropi* with a bootstrap value of 92. The remaining sequences are grouped within clade 3 with bootstrap values of 97: *B. canis*, *B. microti, B. suis, B. ceti, B. pinnipedialis, B. neotomae*, *B. ovis*, *B. melitensis*, *B. pinnipedialis*, *B. abortus*, *B. vulpis, B. inopinata, and diverse Brucella* spp. **(B)** Phylogenetic cladogram of 80 bacteria species. SdhA of *B. ovis* was selected as outgroup to highlight the clear evolutionary separation among Type I, Type IIa and Type IIb MurBs. Sequence alignment and phylogenetic analysis were performed as described in Materials and Methods. The likelihood aLRT (approximate likelihood-ratio test) statistical test and a bootstrap value of 1000 were used.

moiety is less firmly anchored and more exposed to solvent, indicating that it does not play a crucial role in the catalytic incorporation of the nicotinamide. Residues such as N149, Y181, H217 and N235 interact transiently with different atoms of the adenine nucleotide moiety, which suggests it does not significantly impact catalysis. In contrast, the crystal structure for Type I $MurB_{ox}$:$NADP^+$ **(Figure SP13)** reveals that the adenine moiety is more tightly fixed by the Tyr-loop and βαββ motif. This suggests that Type I and Type II MurBs may differ in their affinity for the adenine part of NADPH, potentially affecting access of the nicotinamide to the active site. MD simulations of $MurB_{hq}$:UNAGEP indicate that the enolpyruvyl group of UNAGEP is highly mobile in the active site, possibly due to the reduced state of the flavin (**Figures SP9**). Its UDP moiety also exhibits flexibility (as ADP of NADPH), forming transient interactions with Y242, R251 and H264. Finally, the pyrophosphate half interacts with N235, a position conserved in most MurBs.

These models further envisage a key role for the highly conserved R218 residue in all MurB Types (**Figures SP11**) [74]. Its side chain interacts with the reactive regions of FAD, UNAGEP and NADPH, and is particularly close to the N5 of the isoalloxazine ring (Figs. 7–10 and **SP7-9**). It likely helps to set the redox properties of the cofactor as well as to modulate catalysis. The catalytic residue, S231, H-bonds with the O1E of the enolpyruvyl group of UNAGEP. Likely facilitating proton transfer during the HT from the FAD cofactor (Fig. 7 and SP3). In addition, S231 interacts with the N7N and O7N of the NADPH nicotinamide (Figs. 7 and 10). Another important residue, Q222 -highly conserved in Type II, is in close proximity to the ribose of UNAGEP and the nicotinamide of NADPH (Fig. 10), suggesting it may assist in the correct positioning of substrates in Type II MurBs. R182, conserved across MurB types, interacts with NADPH and is highly mobile, which could further influence substrate binding and catalytic efficiency (Figures SP11-12).

4.4. MurB of B. ovis displays all the characteristics of a type IIa enzyme, and could facilitate the development of inhibitors across different species

MSAs of MurB sequences across various bacterial species, including *B. ovis*, reveal that over 40 % of residues are highly conserved, indicating their crucial role in maintaining the enzyme's structure and/or function. In most *Brucella* the *murB* gene is present in an operon closely resembling that of *B. ovis*, together with other enzymes also involved in PG biosynthesis (Fig. 1B). A similar operon organization is found in many bacteria with Type IIa MurB. In contrast, in some species, the *murB* gene is either not part of any operon or is co-transcribed within a regulon that includes other enzymes [32,34,75]. These findings collectively confirm that the *B. ovis* enzyme shares all key characteristics of Type IIa MurBs.

The conservation of specific residues and motifs within the active site of the MurB family offers potential for developing inhibitors targeting different species. Crystallographic complexes of MurB from *P. aeruginosa* with 3 fragment inhibitors (PDBs: 7OR2, 7ORZ and 7OSQ) illustrate how these inhibitors, all sharing a phenylpyrazole scaffold, bind within the catalytic pocket (**Table SP1**, **Figure SP14**) [21]. The binding of two of them involves two π-π interactions; one between their phenyl rings and the isoalloxazine, and the other between their pyrazole group and Y132. In the third fragment, a triazole replaces one pyrazole, but both π-π interactions with the isoalloxazine are preserved, and an additional H-bond forms with R166. This suggests that Y132 and/or R166 are key to inhibitor binding. Y132, conserved in Type I MurBs, corresponds to N149 in MurB from *B. ovis*. This residue is highly conserved in *Brucella* species and transiently interacts with the non-reactive moieties of UNAGEP and NADPH. However, N149 is less conserved in other Type IIa MurBs. On the other hand, R166 (R182 in *B. ovis*) is a key conserved residue at the active site across all MurB types [74] (Figures SP11-12). The phenylpyrazole scaffold of these inhibitors could provide the basis for the design of compounds with higher affinity and specificity for MurBs. By modifying the pyrazole moiety to specifically interact with N149 it will be possible to aid in the development of targeted inhibitors for this pathogen.

In conclusion, the overexpressed MurB from *B. ovis* is correctly folded, redox active, and capable of interacting with and transforming its substrates. Both experimental and theoretical models demonstrate substrate binding modes that align with expected HT processes. Nonetheless, additional research is needed to confirm the enzyme's overall catalytic parameters, as well as their potential regulation by reaction substrates, which might vary across species. While our results confirm the conservation of key active site residues within MurBs, they also highlight particular features that could be exploited in the development of species-specific antimicrobials targeting the peptidoglycan biosynthetic pathway through this particular enzyme.

CRediT authorship contribution statement

Martha Minjárez-Sáenz: Validation, Methodology, Investigation, Formal analysis, Data curation. **Maribel Rivero:** Methodology, Investigation. **Víctor Correa-Pérez:** Methodology, Investigation. **Sergio Boneta:** Visualization, Validation, Software, Methodology, Investigation, Data curation. **Paula Suárez:** Software, Methodology, Investigation, Formal analysis. **Víctor Polo:** Software, Methodology. **Sheila J. Sadeghi:** Methodology, Investigation. **Inmaculada Yruela:** Visualization, Validation, Software, Methodology, Formal analysis. **Marta Martínez-Júlvez:** Writing – review & editing, Writing – original draft, Visualization, Validation, Supervision, Methodology, Investigation, Formal analysis, Data curation, Conceptualization. **Milagros Medina:** Writing – review & editing, Writing – original draft, Supervision, Resources, Methodology, Investigation, Funding acquisition, Formal analysis, Data curation, Conceptualization.

Data availability

The structural data for the complex $MurB_{ox}$:UNAGEP generated in this study by X-ray crystallography are available in the Protein Data Bank repository (https://www.rcsb.org/) under accession code PDB 9DTK.

Declaration of competing interest

The authors declare no competing interests.

Acknowledgements

This work has been funded by the Spanish State Research Agency and by FEDER (MCIN/AEI-FEDER, Grant PID2022-136369NB-I00) and the Government of Aragón-FEDER (Grants LMP13_21 and E35_23R). X-ray diffraction experiments were performed at BM13-XALOC beamline at ALBA Synchrotron with the collaboration of ALBA staff. Authors acknowledge Dr. Pilar López Ram de Viu for helpful advice with HPLC separations. Authors would like to acknowledge Servicios Generales de

Apoyo a la Investigación-SAI, Universidad de Zaragoza, for support, as well as to the National Facility ICTS, Centro de Supercomputación de Aragón (CESAR), at BIFI-Universidad de Zaragoza, for the instrumentation provided.

Appendix A. Supplementary data

Supplementary data to this article can be found online at https://doi.org/10.1016/j.abb.2025.110288.

References

[1] A. Sonkar, H. Shukla, R. Shukla, J. Kalita, T. Pandey, T. Tripathi, UDP-N-Acetylglucosamine enolpyruvyl transferase (MurA) of *Acinetobacter baumannii* (AbMurA): structural and functional properties, Int. J. Biol. Macromol. 97 (2017) 106–114.
[2] A. El Zoeiby, F. Sanschagrin, R.C. Levesque, Structure and function of the Mur enzymes: development of novel inhibitors, Mol. Microbiol. 47 (1) (2003) 1–12.
[3] H. Barreteau, A. Kovac, A. Boniface, M. Sova, S. Gobec, D. Blanot, Cytoplasmic steps of peptidoglycan biosynthesis, FEMS Microbiol. Rev. 32 (2) (2008) 168–207.
[4] M. Pazos, K. Peters, Peptidoglycan, in: A. Kuhn (Ed.), Bacterial Cell Walls and Membranes, Springer International Publishing, Cham, 2019, pp. 127–168, 978-3-030-18768-2.
[5] T.E. Benson, J.L. Marquardt, A.C. Marquardt, F.A. Etzkorn, C.T. Walsh, Overexpression, purification, and mechanistic study of UDP-N-acetylenolpyruvylglucosamine reductase, Biochemistry 32 (8) (1993) 2024–2030.
[6] K. Mehta, M. Khambete, A. Abhyankar, A. Omri, Anti-tuberculosis mur inhibitors: structural insights and the way ahead for development of novel agents, Pharmaceuticals 16 (3) (2023).
[7] A.M. Dhalla, J. Yanchunas, H.T. Ho, P.J. Falk, J.J. Villafranca, J.G. Robertson, Steady-state kinetic mechanism of *Escherichia coli* UDP-N-acetylenolpyruvylglucosamine reductase, Biochemistry 34 (16) (1995) 5390–5402.
[8] T.E. Benson, C.T. Walsh, V. Massey, Kinetic characterization of wild-type and S229A mutant MurB: evidence for the role of Ser 229 as a general acid, Biochemistry 36 (4) (1997) 796–805.
[9] T.E. Benson, C.T. Walsh, J.M. Hogle, X-ray crystal structures of the S229A mutant and wild-type MurB in the presence of the substrate enolpyruvyl-UDP-N-acetylglucosamine at 1.8-A resolution, Biochemistry 36 (4) (1997) 806–811.
[10] M.J. Axley, R. Fairman, J. Yanchunas, J.J. Villafranca, J.G. Robertson, Spectroscopic properties of *Escherichia coli* UDP-N-acetylenolpyruvylglucosamine reductase, Biochemistry 36 (4) (1997) 812–822.
[11] D.R. Sylvester, E. Alvarez, A. Patel, K. Ratnam, H. Kallender, N.G. Wallis, Identification and characterization of UDP-N-acetylenolpyruvylglucosamine reductase (MurB) from the Gram-positive pathogen *Streptococcus pneumoniae*, Biochem. J. 355 (Pt 2) (2001) 431–435.
[12] S. Nishida, K. Kurokawa, M. Matsuo, K. Sakamoto, K. Ueno, K. Kita, K. Sekimizu, Identification and characterization of amino acid residues essential for the active site of UDP-N-acetylenolpyruvylglucosamine reductase (MurB) from *Staphylococcus aureus*, J. Biol. Chem. 281 (3) (2006) 1714–1724.
[13] Y. Yang, A. Severin, R. Chopra, G. Krishnamurthy, G. Singh, W. Hu, D. Keeney, K. Svenson, P.J. Petersen, P. Labthavikul, D.M. Shlaes, B.A. Rasmussen, A.A. Failli, J.S. Shumsky, K.M. Kutterer, A. Gilbert, T.S. Mansour, 3,5-dioxopyrazolidines, novel inhibitors of UDP-N- acetylenolpyruvylglucosamine reductase (MurB) with activity against gram-positive bacteria, Antimicrob. Agents Chemother. 50 (2) (2006) 556–564.
[14] M.W. Chen, B. Lohkamp, R. Schnell, J. Lescar, G. Schneider, Substrate Channel flexibility in *Pseudomonas aeruginosa* MurB accommodates two distinct substrates, PLoS One 8 (6) (2013) e66936.
[15] T.A. Ewing, M.W. Fraaije, A. Mattevi, W.J.H. van Berkel, The VAO/PCMH flavoprotein family, Arch. Biochem. Biophys. 632 (2017) 104–117.
[16] D. Kumar, N. Sarkar, K.K. Roy, D. Bisht, B. Mandal, M. Rajagopal, Y.N. Dey, The potential of mur enzymes as targets for antimicrobial drug discovery, Curr. Drug Targets 24 (8) (2023) 627–647.
[17] M.A. Haque, M. Singh, M.K. Tripathi, A.S. Ethayathulla, P. Kaur, Identification of natural small molecule modulators of MurB from *Salmonella enterica* serovar Typhi Ty2 strain using computational and biophysical approaches, Proteins 91 (3) (2023) 363–379.
[18] S.M.H. Sanad, A.A.M. Abdelsalam, A.A. Gamal Eldin, E.H. Abdelfattah, F.R. M. Hussein, N.G. Mohammed, N.A.S. Taha, A.E.M. Mekky, Synthesis of new bis (pyrazolo[1,5-a]pyrimidines) linked to different spacers as potential MurB inhibitors, Chem. Biodivers. 20 (6) (2023) e202300546.
[19] A. Verma, V. Kumar, B. Naik, J. Masood Khan, P. Singh, P. Erik Joakim Saris, S. Gupta, Screening and molecular dynamics simulation of compounds inhibiting MurB enzyme of drug-resistant, Saudi J. Biol. Sci. 30 (8) (2023) 103730.
[20] M. Kumar, M.A. Haque, P. Kaur, Computational and biophysical approaches to identify cell wall-associated modulators in *Salmonella enterica* serovar typhi, Methods Mol. Biol. 2727 (2024) 35–55.
[21] M. Acebrón-García-de-Eulate, J. Mayol-Llinàs, M.T.O. Holland, S.Y. Kim, K. P. Brown, C. Marchetti, J. Hess, O. Di Pietro, V. Mendes, C. Abell, R.A. Floto, A. G. Coyne, T.L. Blundell, Discovery of novel inhibitors of uridine diphosphate -*N*-acetylenolpyruvylglucosamine reductase (MurB) from *Pseudomonas aeruginosa*, an opportunistic infectious agent causing death in cystic fibrosis patients, J. Med. Chem. 65 (3) (2022) 2149–2173.
[22] M. Kumari, N. Subbarao, Identification of novel multitarget antitubercular inhibitors against mycobacterial peptidoglycan biosynthetic Mur enzymes by structure-based virtual screening, J. Biomol. Struct. Dyn. 40 (18) (2022) 8185–8196.
[23] V. Hervin, V. Roy, L.A. Agrofoglio, Antibiotics and antibiotic resistance-mur ligases as an antibacterial target, Molecules 28 (24) (2023).
[24] T.E. Benson, C.T. Walsh, J.M. Hogle, The structure of the substrate-free form of MurB, an essential enzyme for the synthesis of bacterial cell walls, Structure 4 (1) (1996) 47–54.
[25] M.J. Pucci, L.F. Discotto, T.J. Dougherty, Cloning and identification of the *Escherichia coli* murB DNA sequence, which encodes UDP-N-acetylenolpyruvoylglucosamine reductase, J. Bacteriol. 174 (5) (1992) 1690–1693.
[26] K.L. Constantine, L. Mueller, V. Goldfarb, M. Wittekind, W.J. Metzler, J. Yanchunas, J.G. Robertson, M.F. Malley, M.S. Friedrichs, B.T. Farmer, Characterization of $NADP^+$ binding to perdeuterated MurB: backbone atom NMR assignments and chemical-shift changes, J. Mol. Biol. 267 (5) (1997) 1223–1246.
[27] K. Eniyan, S. Dharavath, R. Vijayan, U. Bajpai, S. Gourinath, Crystal structure of UDP-N-acetylglucosamine-enolpyruvate reductase (MurB) from *Mycobacterium tuberculosis*, Biochim. Biophys. Acta, Proteins Proteomics 1866 (3) (2018) 397–406.
[28] T.E. Benson, M.S. Harris, G.H. Choi, J.I. Cialdella, J.T. Herberg, J.P. Martin, E. T. Baldwin, A structural variation for MurB: X-ray crystal structure of *Staphylococcus aureus* UDP-N-acetylenolpyruvylglucosamine reductase (MurB), Biochemistry 40 (8) (2001) 2340–2350.
[29] L.M. Schulz, P. Rothe, S. Halbedel, A. Gründling, J. Rismondo, Imbalance of peptidoglycan biosynthesis alters the cell surface charge of *Listeria monocytogenes*, Cell Surf 8 (2022) 100085.
[30] M.E. Auldridge, H. Cao, S. Sen, L.P. Franz, C.A. Bingman, R.M. Yennamalli, G. N. Phillips, D. Mead, E.J. Steinmetz, LucY: a versatile new fluorescent reporter protein, PLoS One 10 (4) (2015) e0124272.
[31] M.K. Kim, M.K. Cho, H.E. Song, D. Kim, B.H. Park, J.H. Lee, G.B. Kang, S.H. Kim, Y. J. Im, D.S. Lee, S.H. Eom, Crystal structure of UDP-N-acetylenolpyruvylglucosamine reductase (MurB) from *Thermus caldophilus*, Proteins 66 (3) (2007) 751–754.
[32] M. Minjárez-Sáenz, M. Martínez-Júlvez, I. Yruela, M. Medina, Mining the flavoproteome of *Brucella ovis*, the brucellosis causing agent in Ovis aries, Microbiol. Spectr. 10 (2) (2022) e0229421.
[33] N. Picard-Hagen, X. Berthelot, J.L. Champion, L. Eon, F. Lyazrhi, M. Marois, M. Peglion, A. Schuster, C. Trouche, B. Garin-Bastuji, Contagious epididymitis due to *Brucella ovis*: relationship between sexual function, serology and bacterial shedding in semen, BMC Vet. Res. 11 (2015) 125.
[34] J. Mingorance, J. Tamames, M. Vicente, Genomic channeling in bacterial cell division, J. Mol. Recogn. 17 (5) (2004) 481–487.
[35] P. Macheroux, UV-visible spectroscopy as a tool to study flavoproteins, Methods Mol. Biol. 131 (1999) 1–7.
[36] P. Ferreira, M. Medina, Anaerobic stopped-flow spectrophotometry with photodiode array detection in the presteady state: an application to elucidate oxidoreduction mechanisms in flavoproteins, Methods Mol. Biol. 2280 (2021) 135–155.
[37] M. Medina, M. Martinez-Julvez, J.K. Hurley, G. Tollin, C. Gomez-Moreno, Involvement of glutamic acid 301 in the catalytic mechanism of ferredoxin-NADP(+) reductase from *Anabaena* PCC 7119, Biochemistry 37 (9) (1998) 2715–2728.
[38] E. Maklashina, G. Cecchini, Determination of flavin potential in proteins by xanthine/xanthine oxidase method, Bio Protoc 10 (7) (2020) e3571.
[39] S.L. Christgen, S.M. Becker, D.F. Becker, Methods for determining the reduction potentials of flavin enzymes, Methods Enzymol. 620 (2019) 1–25.
[40] V.R. Dodhia, C. Sassone, A. Fantuzzi, G.D. Nardo, S.J. Sadeghi, G. Gilardi, Modulating the coupling efficiency of human cytochrome P450 CYP3A4 at electrode surfaces through protein engineering, Electrochem. Commun. 10 (2008) 1744–1747.
[41] R.A. Anwar, M. Vlaovic, Purification of UDP-N-acetylenolpyruvoylglucosamine reductase from *Escherichia coli* by affinity chromatography, its subunit structure and the absence of flavin as the prosthetic group, Can. J. Biochem. 57 (2) (1979) 188–196.
[42] J. Sancho, The stability of 2-state, 3-state and more-state proteins from simple spectroscopic techniques… plus the structure of the equilibrium intermediates at the same time, Arch. Biochem. Biophys. 531 (1–2) (2013) 4–13.
[43] W. Kabsch Xds, Acta Crystallogr. D Biol. Crystallogr. 66 (Pt 2) (2010) 125–132.
[44] P. Evans, Scaling and assessment of data quality, Acta Crystallogr. D Biol. Crystallogr. 62 (Pt 1) (2006) 72–82.
[45] CCP4, The CCP4 suite: programs for protein crystallography, Acta Crystallogr. D Biol. Crystallogr. 50 (Pt 5) (1994) 760–763.
[46] M.D. Winn, C.C. Ballard, K.D. Cowtan, E.J. Dodson, P. Emsley, P.R. Evans, R. M. Keegan, E.B. Krissinel, A.G. Leslie, A. McCoy, S.J. McNicholas, G.N. Murshudov, N.S. Pannu, E.A. Potterton, H.R. Powell, R.J. Read, A. Vagin, K.S. Wilson, Overview of the CCP4 suite and current developments, Acta Crystallogr. D Biol. Crystallogr. 67 (Pt 4) (2011) 235–242.
[47] A. Vagin, A. Teplyakov, MOLREP: an automated program for molecular replacement, J. Appl. Crystallogr. 30 (1997) 1022–1025.
[48] J. Jumper, R. Evans, A. Pritzel, T. Green, M. Figurnov, O. Ronneberger, K. Tunyasuvunakool, R. Bates, A. Žídek, A. Potapenko, A. Bridgland, C. Meyer, S.A. A. Kohl, A.J. Ballard, A. Cowie, B. Romera-Paredes, S. Nikolov, R. Jain, J. Adler, D. Hassabis, Highly accurate protein structure prediction with AlphaFold, Nature 596 (7873) (2021) 583–589.

[49] G.N. Murshudov, P. Skubák, A.A. Lebedev, N.S. Pannu, R.A. Steiner, R.A. Nicholls, M.D. Winn, F. Long, A.A. Vagin, REFMAC5 for the refinement of macromolecular crystal structures, Acta Crystallogr. D Biol. Crystallogr. 67 (Pt 4) (2011) 355–367.
[50] P. Emsley, B. Lohkamp, W.G. Scott, K. Cowtan, Features and development of coot, Acta Crystallogr. D Biol. Crystallogr. 66 (Pt 4) (2010) 486–501.
[51] P.D. Adams, P.V. Afonine, G. Bunkoczi, V.B. Chen, I.W. Davis, N. Echols, J. J. Headd, L.W. Hung, G.J. Kapral, R.W. Grosse-Kunstleve, A.J. McCoy, N. W. Moriarty, R. Oeffner, R.J. Read, D.C. Richardson, J.S. Richardson, T. C. Terwilliger, P.H. Zwart, PHENIX: a comprehensive Python-based system for macromolecular structure solution, Acta Crystallogr. D Biol. Crystallogr. 66 (Pt 2) (2010) 213–221.
[52] V.B. Chen, W.B. Arendall, J.J. Headd, D.A. Keedy, R.M. Immormino, G.J. Kapral, L. W. Murray, J.S. Richardson, D.C. Richardson, MolProbity: all-atom structure validation for macromolecular crystallography, Acta Crystallogr. D Biol. Crystallogr. 66 (Pt 1) (2010) 12–21.
[53] M.H. Olsson, C.R. Søndergaard, M. Rostkowski, J.H. Jensen, PROPKA3: consistent treatment of internal and surface residues in empirical pKa predictions, J. Chem. Theor. Comput. 7 (2) (2011) 525–537.
[54] M.J. Abraham, T. Murtola, R. Schulz, S. Páll, J.C. Smith, B. Hess, E. Lindahl, GROMACS: high performance molecular simulations through multi-level parallelism from laptops to supercomputers, SoftwareX 1–2 (2015) 19–25.
[55] Y. Duan, C. Wu, S. Chowdhury, M.C. Lee, G. Xiong, W. Zhang, R. Yang, P. Cieplak, R. Luo, T. Lee, J. Caldwell, J. Wang, P. Kollman, A point-charge force field for molecular mechanics simulations of proteins based on condensed-phase quantum mechanical calculations, J. Comput. Chem. 24 (16) (2003) 1999–2012.
[56] T. Lu, F. Chen, Multiwfn: a multifunctional wavefunction analyzer, J. Comput. Chem. 33 (5) (2012) 580–592.
[57] M.J. Frisch, G. Trucks, H.B. Schlegel, G.E. Scuseria, M.A. Robb, J. Cheeseman, G. Scalmani, V. Barone, B. Mennucci, G.A. Petersson, H. Nakatsuji, M. Caricato, X. Li, H.P. Hratchian, A.F. Izmaylov, J. Bloino, G. Zheng, J. Sonnenberg, M. Hada, D. Fox, Gaussian 09 Revision A.1, Gaussian Inc, 2009.
[58] J. Wang, W. Wang, P.A. Kollman, D.A. Case, Automatic atom type and bond type perception in molecular mechanical calculations, J. Mol. Graph. Model. 25 (2) (2006) 247–260.
[59] A.W. Sousa da Silva, W.F. Vranken, Acpype - AnteChamber PYthon parser interfacE, BMC Res. Notes 5 (2012) 367.
[60] B. Hess, P-LINCS: a parallel linear constraint solver for molecular simulation, J. Chem. Theor. Comput. 4 (1) (2008) 116–122.
[61] R.T. McGibbon, K.A. Beauchamp, M.P. Harrigan, C. Klein, J.M. Swails, C. X. Hernández, C.R. Schwantes, L.P. Wang, T.J. Lane, V.S. Pande, MDTraj: a modern open library for the analysis of molecular dynamics Trajectories, Biophys. J. 109 (8) (2015) 1528–1532.
[62] W.L. Delano, PyMOL: an open-source molecular graphics tool, CCP4 Newsletter On Protein Crystallogr. 40 (2002) 82–92.
[63] N.A. O'Leary, M.W. Wright, J.R. Brister, S. Ciufo, D. Haddad, R. McVeigh, B. Rajput, B. Robbertse, B. Smith-White, D. Ako-Adjei, A. Astashyn, A. Badretdin, Y. Bao, O. Blinkova, V. Brover, V. Chetvernin, J. Choi, E. Cox, O. Ermolaeva, K. D. Pruitt, Reference sequence (RefSeq) database at NCBI: current status, taxonomic expansion, and functional annotation, Nucleic Acids Res. 44 (D1) (2016) D733–D745.
[64] T. Paysan-Lafosse, M. Blum, S. Chuguransky, T. Grego, B.L. Pinto, G.A. Salazar, M. L. Bileschi, P. Bork, A. Bridge, L. Colwell, J. Gough, D.H. Haft, I. Letunić, A. Marchler-Bauer, H. Mi, D.A. Natale, C.A. Orengo, A.P. Pandurangan, C. Rivoire, A. Bateman, InterPro in 2022, Nucleic Acids Res. 51 (D1) (2023) D418–D427.
[65] G.E. Crooks, G. Hon, J.M. Chandonia, S.E. Brenner, WebLogo: a sequence logo generator, Genome Res. 14 (6) (2004) 1188–1190.
[66] K. Tamura, G. Stecher, S. Kumar, MEGA11: molecular evolutionary genetics analysis version 11, Mol. Biol. Evol. 38 (7) (2021) 3022–3027.
[67] H. Kishino, M. Hasegawa, Evaluation of the maximum likelihood estimate of the evolutionary tree topologies from DNA sequence data, and the branching order in hominoidea, J. Mol. Evol. 29 (2) (1989) 170–179.
[68] I. Yruela, C. Moreno-Yruela, C.A. Olsen, Zn^{2+}-Dependent histone deacetylases in plants: structure and Evolution, Trends Plant Sci. 26 (7) (2021) 741–757.
[69] M. Becana, I. Yruela, G. Sarath, P. Catalán, M.S. Hargrove, Plant hemoglobins: a journey from unicellular green algae to vascular plants, New Phytol. 227 (6) (2020) 1618–1635.
[70] F. Lemoine, D. Correia, V. Lefort, O. Doppelt-Azeroual, F. Mareuil, S. Cohen-Boulakia, O. Gascuel, NGPhylogeny.fr: new generation phylogenetic services for non-specialists, Nucleic Acids Res. 47 (W1) (2019) W260–W265.
[71] Y. Zhang, J. Skolnick, TM-align: a protein structure alignment algorithm based on the TM-score, Nucleic Acids Res. 33 (7) (2005) 2302–2309.
[72] K.F. Naqvi, D. Patin, M.S. Wheatley, M.A. Savka, R.C. Dobson, H.M. Gan, H. Barreteau, D. Blanot, D. Mengin-Lecreulx, A.O. Hudson, Identification and partial characterization of a novel UDP-N-acetylenolpyruvoylglucosamine reductase/UDP-N-Acetylmuramate:l-Alanine ligase fusion enzyme from *Verrucomicrobium spinosum* DSM 4136(T), Front. Microbiol. 7 (2016) 362.
[73] A. Mason, N. Agrawal, M.T. Washington, S.A. Lesley, A. Kohen, A lag-phase in the reduction of flavin dependent thymidylate synthase (FDTS) revealed a mechanistic missing link, Chem. Commun. 16 (2006) 1781–1783.
[74] O. Dym, D. Eisenberg, Sequence-structure analysis of FAD-containing proteins, Protein Sci. 10 (9) (2001) 1712–1728.
[75] M.A. Eisenberg, O. Prakash, S.C. Hsiung, Purification and properties of the biotin repressor. A bifunctional protein, J. Biol. Chem. 257 (24) (1982) 15167–15173.